Non-Equilibrium Reaction and Relaxation Dynamics in a Strongly Interacting Explicit Solvent: F + CD_3CN Modelled with a Parallel Multi-state EVB Model

David R. Glowacki,[1,2,3,4]* Andrew J. Orr-Ewing,[1] and Jeremy N. Harvey[5]

[1]*School of Chemistry, University of Bristol, Bristol, BS8 1TS, UK*
[2]*Department of Computer Science, University of Bristol, BS8 1UB, UK*
[3]*PULSE Institute and Department of Chemistry, Stanford University, Stanford, CA 94305, USA*
[4]*SLAC National Accelerator Laboratory, Menlo Park, California 94025, USA*
[5]*Department of Chemistry, KU Leuven, Celestijnenlaan 200F, B-3001 Heverlee*

*drglowacki@gmail.com

Abstract

We describe a parallelized linear-scaling computational framework developed to implement arbitrarily large multi-state empirical valence bond (MS-EVB) calculations within CHARMM and TINKER. Forces are obtained using the Hellman-Feynmann relationship, giving continuous gradients, and good energy conservation. Utilizing multi-dimensional Gaussian coupling elements fit to CCSD(T)-F12 electronic structure theory, we built a 64-state MS-EVB model designed to study the F + $CD_3CN \rightarrow$ DF + CD_2CN reaction in CD_3CN solvent (recently reported in *Science*, 347(6221), 530 (2015)). This approach allows us to build a reactive potential energy surface (PES) whose balanced accuracy and efficiency considerably surpass what we could achieve otherwise. We ran MD simulations to examine a range of observables which follow in the wake of the reactive event: energy deposition in the nascent reaction products, vibrational relaxation rates of excited DF in CD_3CN solvent, equilibrium power spectra of DF in CD_3CN, and time dependent spectral shifts associated with relaxation of the nascent DF. Many of our results are in good agreement with time-resolved experimental observations, providing good evidence for the accuracy of our MS-EVB framework in treating both the solute and solute/solvent interactions. The simulations provide additional insight into the dynamics at sub-picosecond timescales that are difficult to resolve experimentally. In particular, the simulations show that (immediately following deuterium abstraction) the nascent DF finds itself in a non-equilibrium regime in two different respects: (1) it is highly vibrationally excited, with ~23 kcal mol^{-1} localized in the stretch; and (2) not yet hydrogen-bonded to CD_3CN solvent molecules, its post-reaction microsolvation environment is intermediate between the non-interacting gas-phase limit and the solution-phase equilibrium limit. Vibrational relaxation of the nascent DF results in a spectral blue shift, while relaxation of the post-reaction microsolvation environment results in a red shift. These two competing effects mean that the post-reaction relaxation profile is distinct from what is observed when Frank-Condon vibrational excitation of DF occurs within a microsolvation environment initially at equilibrium. Our conclusions, along with the theoretical and parallel software framework presented in this paper, should be more broadly applicable to a range of complex reactive systems.

Introduction

The study of non-equilibrium reaction dynamics in condensed phases remains a fascinating research area. It is well known that vibrationally excited molecules can persist for long enough to be experimentally observed in cases where they are prepared using optical methods,[1-5] with consequences on reaction outcomes.[6-9] In 1991, Hynes and co-workers provided a detailed molecular dynamics description of the mechanism by which vibrational activation on the reactant-side of the transition state gives rise to barrier crossing for thermal S_N2 reactions in solution.[10] The extent to which chemical reactions under *thermal* conditions can lead to vibrationally excited products is an area which, until recently, has been less well studied. Over the last few years, a handful of experimental and theoretical studies have highlighted solution-phase chemical reactions which give rise to products with observable vibrational excitation beyond that which would be expected at thermal equilibrium.[11-19] Alongside these observations, a growing number of studies have shown that the extent of vibrational excitation and its subsequent relaxation dynamics can actually impact reaction outcomes in solvents.[20-22] For example, there is good evidence that thermal reactions as well-known as alkene hydroboration have a Markovnikov/Anti-Markovnikov product ratio which is determined by the extent of nascent vibrational excitation in the short lived addition complex.[12, 23] Recently, it has even been suggested that solute/solvent interactions which take place in the course of transient vibrational relaxation dynamics provide a route to enantioselective amplification.[19]

Accurately simulating reaction dynamics in coupled solute/solvent environments remains a challenge within the field of computational and theoretical chemistry,[14, 16, 24-26] mostly owing to the fact that it is difficult to construct a potential energy surface (PES) whose balanced accuracy and efficiency is sufficient to interpret experiments. Further complications arise according to the fact that experimental dynamic observables ultimately derive from the quantum mechanical properties of molecules, but efficient methods for carrying out full quantum mechanical dynamics simulations of condensed phase systems are not generally available. Most approaches therefore utilize classical mechanics, often invoking correction factors to bring the classical simulations into agreement with the known quantum mechanical results for simple model systems.[27-29] In equilibrium regimes, there are a number of approaches which have been well tested;[27, 30] however, far from equilibrium, the approaches for mapping classical results onto quantum mechanical observables are less developed.[31]

Parameterized force-fields continue to play an important role in computational investigations of the condensed phase.[32] They provide insight into a range of questions spanning biochemical systems, materials science, and solvent dynamics, but they also have a number of

well-known shortcomings. From the perspective of the work presented in this paper, the most significant shortcoming arises from the fact that force-field parameterization schemes tend to focus on equilibrium properties – i.e., in the vicinity of energy minima where anharmonicity is very small. As a result, they do an excellent job near stationary point minima; however, outside this narrow region they are unable to accurately answer a range of experimentally relevant questions. In particular, the formation and breaking of chemical bonds usually occurs in regions which are far from stationary point minima, requiring the localization of several quanta of vibrational excitation in a particular bond.[33] Similarly, relaxation dynamics often occur in regions of phase space that are far from the parameterized minima. Detailed studies of phenomena that occur far from the stationary point minima (e.g., reaction and relaxation dynamics) therefore have an important role to play in refining force-field type approaches.

Advances in experimental techniques provide increasingly detailed measurements in condensed phase systems, providing excellent tests of corresponding computational approaches.[6, 34-38] The last decade or so has seen a number of attempts by a range of workers to efficiently and accurately simulate chemical reaction dynamics in condensed-phase environments using multi-state molecular mechanics and multi-state empirical valence bond (MS-EVB) approaches.[19, 39-49] Such approaches represent important molecular configurations using diabatic valence bond states, which are coupled using any of a wide range of schemes.[42, 50-53] So far, such approaches have largely been confined to simulation of reactions in enzymes, and for proton transfer in aqueous environments.

In recent work we have investigated polyatomic reaction dynamics of solutes which couple weakly to organic solvents:[14, 54] namely, $CN + C_6H_{12} \rightarrow HCN + C_6H_{11}$ in dichloromethane solvent,[13, 17, 18] and $CN + C_4H_8O \rightarrow HCN + C_4H_7O$ in tetrahydrofuran (C_4H_8O) solvent.[15] In both cases, our reaction dynamics studies were focussed on unravelling the dynamics in the post-transition state region – i.e., the production and subsequent relaxation of vibrationally hot products formed during the abstraction event. These studies exploited EVB force fields along with the recently developed BXD rare event acceleration algorithm, allowing us to generate statistically meaningful non-equilibrium dynamics in the post transition state region.[55] To the best of our knowledge, these theoretical molecular dynamics (MD) investigations of non-equilibrium solution phase bimolecular reaction dynamics were amongst the first of their kind. Through detailed comparison with ultrafast spectroscopy experiments, we were able to provide microscopic detail into how the relaxation dynamics which follow a chemical reaction differ from the relaxation dynamics which follow vibrational relaxation in an equilibrated microsolvation environment.[24]

This paper describes simulations of F atom abstraction reactions in CD_3CN solvent to give $DF + CD_2CN$,[11] in which the solute/solvent coupling is considerably stronger than in our previous studies. An accurate treatment of the dynamics in this stronger coupling regime requires a more complicated simulation framework than that utilized previously. Specifically, we used a locally modified version of the CHARMM program suite[56] to build a parallel 64-state EVB model from Gaussian coupling elements whose parameters were fit against CCSD(T)-F12 electronic structure theory calculations (we have recently undertaken a nearly identical MS-EVB parallelization of TINKER[19]). The net result is a generalized parallel simulation framework for accurately modelling the dynamics of chemical reactions, as well as the subsequent relaxation dynamics.

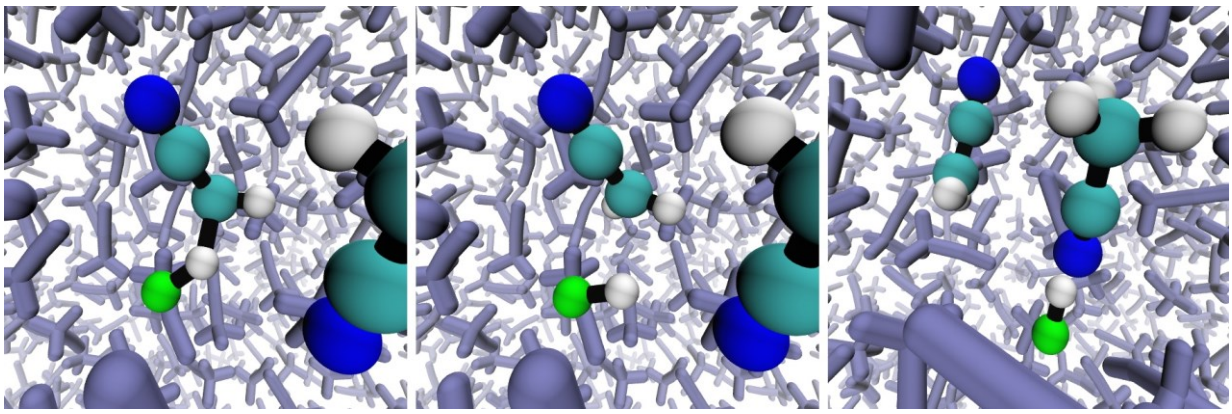

Figure 1: Snapshots from MD simulations. The left hand panel shows the fluorine radical embedded in CD_3CN solvent prior to abstraction, the middle panel shows the moment immediately following abstraction to form DF, and the right hand panel shows the diatomic DF product hydrogen-bonded to one of the solvent molecules

Figure 1 shows a schematic of the reaction we investigate in this article, i.e.:

$$F + CD_3CN \rightarrow DF + CD_2CN \qquad (R1)$$

Within CD_3CN solvent, (R1) may be decomposed into the following elementary steps:

$$F + CD_3CN \rightarrow DF^* + CD_2CN \qquad (R1a)$$

$$DF^* \rightarrow DF \qquad (R1b)$$

The simulations described in this paper reveal that the transient dynamics of the nascent DF* which is produced in (R1a) and relaxed in (R1b) result from a set of interlinked physical observables, including: (1) DF vibrational anharmonicity [which depends on both the force field and the energy content of the DF solute]; (2) the time-dependent solute/solvent spectral overlap; (3) the magnitude of the solute/solvent coupling; and (4) the timescale at which the microsolvation environment of the nascent DF approaches equilibrium. In organizing this paper, we have attempted to decompose the effects responsible for the observed DF dynamics obtained in our simulations by focussing on the various elements described above.

This paper is broadly divided into two different sections. The first section focuses on the PES we developed to model (R1a) and (R1b). We outline electronic structure theory calculations

[density function theory (DFT) and coupled cluster with singles, doubles, and perturbative triples (CCSD(T))] carried out to model two important regions of the PES: the abstraction path, and also post-reaction complexes between DF and CD_3CN solvent molecules. The electronic structure theory energies were then used to fit an MS-EVB model. This approach allows us to accurately and efficiently treat the electronic quantum mechanics of both the abstraction dynamics and the coupling between the DF solute and the CD_3CN solvent molecules. The second section focuses on classical molecular dynamics simulations which we carried out to describe the nuclear reorganization that takes place in (R1). First, we describe our treatment of DF anharmonicity. Second, we outline the results obtained from non-equilibrium vibrational relaxation dynamics (NE-VRD) simulations – i.e., simulations in which DF, excited according to the Frank-Condon principle, relaxes within a CD_3CN microsolvation environment that is initially at equilibrium. Here, we pay particular attention to how the DF relaxation timescales depend on solute/solvent spectral overlap, and the strength of solvent/solute coupling. Third, we describe non-equilibrium post-reaction solvation dynamics (NE-PRSD) simulations designed to analyse the time-dependent relaxation of DF's post-reaction microsolvation environment immediately following its formation in the wake of chemical reaction. Finally, we describe non-equilibrium reactive dynamics (NE-RxD) simulations of (R1) in its entirety, showing how the observed time-dependent spectra depend on the effects outlined previously. The microscopic picture that emerges from these simulations reveals a complicated time-dependent spectral profile of the nascent DF, which results from two opposing effects: a fast red shift occurs as DF's post-reaction solvation environment relaxes, forming complexes between DF and neighboring solvent molecules, and a competing blue shift occurs as DF loses its vibrational energy to the solvent.

Potential Energy Surfaces

Electronic Structure calculations

Dynamics simulations, and product energy deposition in particular, are very sensitive to the shape of the PES.[57, 58] Similarly, it has been shown that vibrational energy relaxation rates of simple solutes depend on the coupling of anharmonic modes in the solute and solvent PES.[2, 59, 60] Accordingly, the first part of this study involved obtaining an accurate representation of: (1) the abstraction region of the F + CD_3CN PES, which determines product energy deposition; and (2) post-reaction complexes which may be formed following abstraction (i.e., $CD_2CN\cdots DF$ and $CD_3CN\cdots DF$). Contour plots of both these regions of the PES are shown in Fig 2.

To determine a set of geometries and accurate corresponding energies in these different regions of the PES, we utilized the following procedure: structures for the separated reactants and

products, the CD_3CN•F reactant complex, the CD_2CN—DF product complex, the solvent complex CD_3CN—DF and the F···D···CD_2CN abstraction TS were optimized using density functional theory, with the M06-2X functional and the 6-311+G(d,p) basis set within the Gaussian program suite.[61] Frequency calculations confirmed that the optimized structures were indeed minima or saddlepoints. Additional structures were generated at points lying close to the minimum energy path for deuterium abstraction. These were obtained by optimizing the structure of acetonitrile while holding the C-D bond length fixed at a set of values ranging from 0.8 Å to 2.8 Å, in steps of 0.1 Å, and are shown in Fig 2. This was done using the same M06-2X functional and basis set, and with careful checking for lower-energy unrestricted solutions at larger C-D distances. Then the fluorine atom was positioned collinearly along the C-D bond direction at a set of distances. Additional structures corresponding to distorted CD_3CN—DF species were obtained in two ways. First, this complex was reoptimized while holding the D—F distance frozen at values between 0.80 and 1.1 Å, in steps of 0.05 Å. Inspection of these structures showed that the internal structure of the CD_3CN moiety barely changed with respect to equilibrium. Hence additional structures, also shown in Fig 2, were obtained by varying the N-D and D-F distances while holding other coordinates fixed at those for the equilibrium CD_3CN—DF complex. Single-point energies at all these structures were computed using the CCSD(T) method with explicit treatment of electron-electron correlation using the F12-b ansatz within the MOLPRO program suite.[62-64] The cc-pVTZ basis set was used for D and C atoms, and the aug-cc-pVTZ basis for N and F. Appropriate auxiliary basis sets from the aug-cc-pVTZ family were used for the F12 corrections. In what follows, we report relative energies based on electronic energies from our coupled-cluster calculations – we do not include a vibrational zero-point energy correction unless mentioned otherwise.

Table 1 shows results obtained using the electronic structure methods discussed above. Our main motivation for choosing the M06-2X functional is that it returns a TS energy similar to that obtained with coupled-cluster theory. Table 1 shows that the first species along the reaction coordinate is a weak pre-reaction complex between the fluorine and the lone pair of acetonitrile. The reaction then proceeds over a low-lying abstraction TS which is early (C—D and D—F distances of 1.131 Å and 1.493 Å respectively) and nearly linear in structure (C—D—F angle of 162°). Both the product radical and CD_3CN form strong hydrogen bonds with DF. This leads to a slight elongation of the DF bond, from 0.918 Å in isolated DF to 0.932 Å in the DF–CD_3CN complex. The CCSD(T) calculations predict that this complex is bound by 9.1 kcal mol^{-1}. As will be shown later, the existence of strong hydrogen bonds between nascent DF and the cyano moiety

of the CD_3CN solvent molecules is important to the dynamics results. Table 2 shows vibrational frequencies for the stationary points in Table 1.

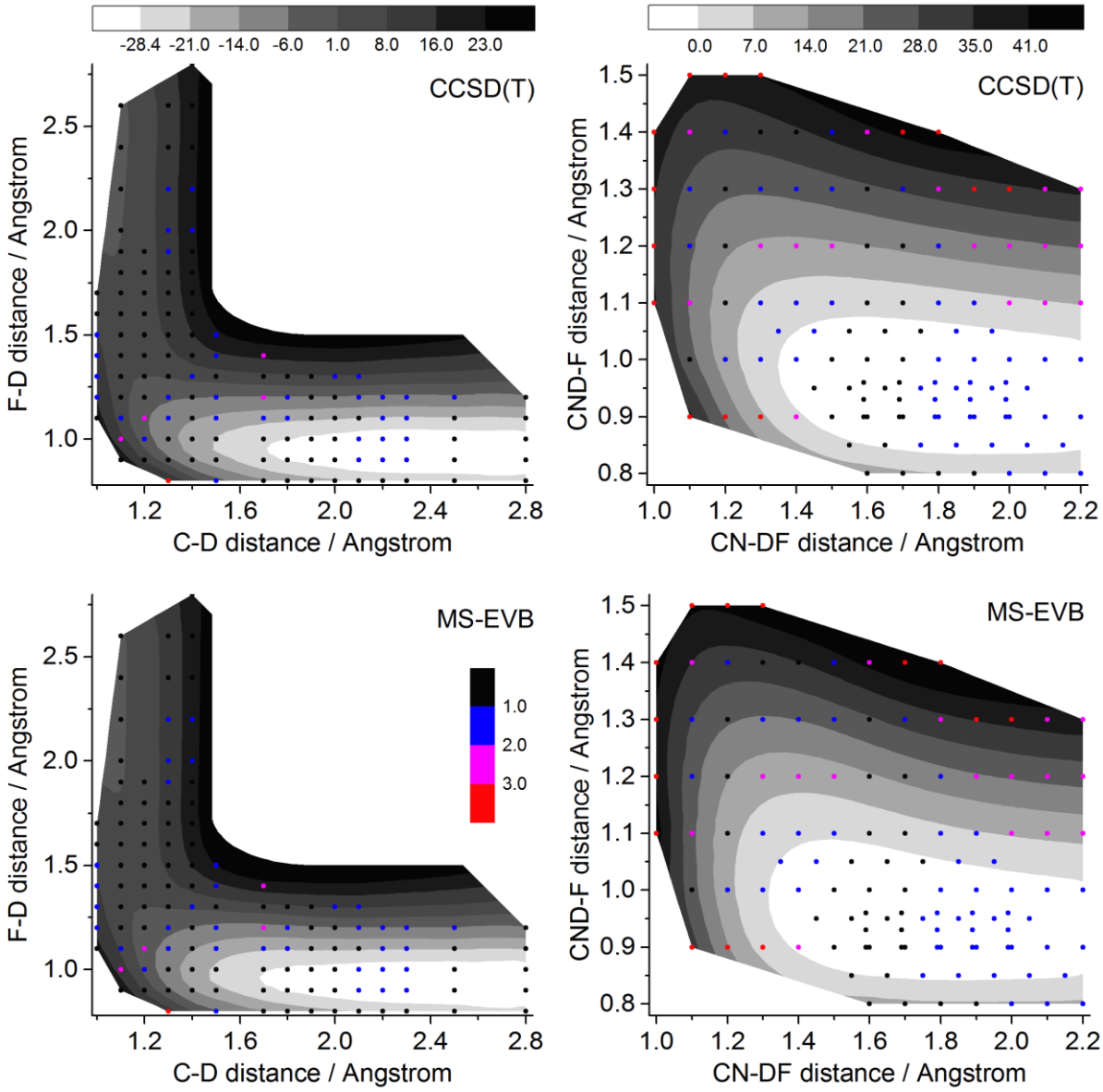

Figure 2: Contour plots in the top panel show interpolated CCSD(T) PESs (energy in units of kcal mol^{-1}) for geometries along the abstraction pathway (left-hand side, energies relative to separated F + CD_3CN), and in the region of the post reaction CD_3CN-DF complex (right-hand side, energies relative to separated DF + CD_3CN). The bottom panel shows corresponding MS-EVB PES contours for energy evaluations at the same geometries. The points in each plot indicate the geometries at which CCSD(T) energy evaluations were undertaken; the color at a particular point indicates the magnitude of the difference between the CCSD(T) energy and the fitted MS-EVB energy (in units of kcal mol^{-1}).

Table 1: Calculated potential energies (in kcal mol^{-1}) for species involved in the F + CD_3CN reaction, and subsequent interaction of DF with solvent molecules. [(a)] Energies calculated at the M06-2X structures; [(b)] Energy relative to CD_3CN + DF.

Species	E_{rel}(M06-2X)	E_{rel}(M06-2X+zpe)	E_{rel}(CCSD(T)-F12)[(a)]
F + CD_3CN	0.0	0.0	0.0
CD_3CN•F	–3.7	–3.3	–2.1
TS	1.3	–0.7	2.5
CD_2CN—DF	–43.1	–44.3	–45.1
CD_2CN + DF	–34.3	–37.3	–36.8
CD_3CN—DF[(b)]	–9.6	–7.7	–9.1

Table 2: Calculated M06-2X/6-311+G(d,p) frequencies (in cm^{-1}) for species involved in the F + CD_3CN reaction.

Species	Vibrational frequencies
DF	3050
CD_3CN	352, 354, 844, 864, 864, 1062, 1063, 1134, 2208, 2339, 2341, 2423
CD_2CN	344, 399, 540, 853, 925, 1168, 2215, 2312, 2461
CD_2CN—DF	41, 51, 180, 346, 399, 457, 460, 548, 855, 930, 1167, 2250, 2312, 2464, 2831
CD_3CN—DF	46, 48, 184, 357, 358, 479, 479, 853, 866, 866, 1059, 1060, 1135, 2209, 2342, 2344, 2446, 2799

Multi-State EVB calculations

Running direct dynamics using the CCSD(T) methods described above would have been prohibitively expensive. It may have been possible to exploit recent advances in computational efficiency to perform DFT calculations on this system,[65, 66] but the cost would have nevertheless been significant, and would not have yielded satisfactory statistics for interpreting the dynamics. Consequently, we sought other means to develop an accurate representation of the electronic structure results discussed above. Building on previous work, we fit an MS-EVB model to the CCSD(T) results. In the MS-EVB approach,[53] basis functions that effectively correspond to different molecular valence states are used to formulate a Hamiltonian matrix $\mathbf{H}(\mathbf{q})$. The diagonal elements of this matrix, $V_i(\mathbf{q})$, correspond to the molecular mechanics energy of a particular valence state specified by a particular connectivity. The off-diagonal elements $H_{ij}(\mathbf{q})$ describe the coupling between different molecular configurations. Similar to our previous work, the off-diagonal elements are a function of the system coordinates $\mathbf{q}$.

To reproduce the electronic structure results in Fig 2, and to account for the fact that the nascent DF formed following D abstraction from CD_3CN is able to form complexes with any of n solvent molecules included within the simulation, we required four different types of valence states. These are shown in Fig 3, for the simplest illustrative case, with $n = 2$ solvent molecules. State 1 shows a fluorine radical nestled between two distinct solvent molecules. In principle, the fluorine could abstract any of 3 deuterium atoms from any of the n solvent molecules, resulting in $3n$ possible abstraction processes. In practice, to reduce the computational expense of the simulations, the fluorine is allowed to abstract a single D atom from a particular nearby solvent molecule. The other $n - 1$ solvent molecules are not reactive, but they nevertheless interact with the reacting system as it progresses along the reaction coordinate from reactants to products.[67] State 2 corresponds to the products formed following the abstraction process. The nascent DF may subsequently form a post-reaction complex – either with its radical co-product, or with any of the other $(n - 1)$ solvent molecules within the simulation. State 3 corresponds to deuteron

transfer from DF to the nitrogen atom of its co-radical product, and state 4 corresponds to deuteron transfer from DF to the nitrogen atom of the other solvent molecule. In general, there are (n – 1) replicas of state 4, allowing DF to transfer a proton to every non-reactive solvent molecule in the simulation. As discussed further below, states 3 and 4 allow construction of a PES in good agreement with CCSD(T) calculations, and play a critical role in quantitatively modeling the energy transfer rate. (Kiefer *et al*. recently described a similar approach to investigate spectral shifts associated with hydrogen bonded complexes.[48])

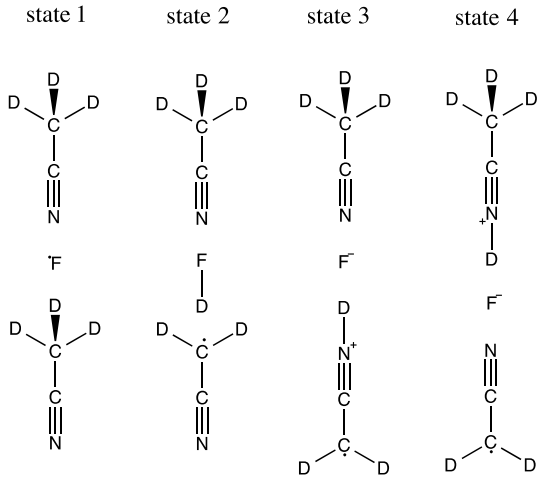

Figure 3: Schematic representation of the diabatic states utilized in our MS-EVB model. For simplicity, we have shown the states that arise for a fluorine radical embedded in a "bath" composed of only two CD_3CN solvent molecules. For the simulations detailed in the text, F was embedded in n = 62 solvent molecules

In our previous work on CN + C_6H_{12} abstraction reactions, **H**(**q**) was built utilizing two states (i.e., a 2 × 2 matrix). For reasons elaborated below, the 2 × 2 approach is inadequate for the present system. Instead, we used a rather different approach: **H**(**q**) for a fluorine radical embedded in n solvent molecules has a dimension of (n + 2) × (n + 2), with the following structure:

$$\mathbf{H} = \begin{bmatrix} V_1+\varepsilon_1 & H_{12} & 0 & 0 & \cdots & 0 \\ 0 & V_2+\varepsilon_2 & H_{23} & H_{24} & \cdots & H_{24} \\ 0 & H_{23} & V_3+\varepsilon_3 & 0 & \cdots & 0 \\ 0 & H_{24} & 0 & V_4+\varepsilon_4 & \cdots & 0 \\ \vdots & \vdots & \vdots & \vdots & \ddots & 0 \\ 0 & H_{24} & 0 & 0 & 0 & V_{n+2}+\varepsilon_{n+2} \end{bmatrix} \quad (1)$$

where the diagonal elements V_1, V_2, and V_3 correspond to the respective energies of states 1, 2, and 3 in Fig 3. Diagonal elements with indices spanning $V_4 \ldots V_{n+2}$ correspond to the diabatic energies of the different replicas of state 4 in Fig. 3, i.e. for deuteron transfer from DF to each of the (n – 1) solvent molecules in the simulation. The ε values are constant diagonal energy shifts chosen to reproduce reaction energies. To calculate the diagonal elements, we utilized the functional forms and parameters available in the Merck Molecular Mechanics force field[68] with

some important modifications. In particular, the default van der Waals parameters of the D atom in DF were changed to correspond to those of the H in H_2O in order to give the appropriate post-reaction complex stabilization energy (discussed below). The equilibrium bond distance for DF was specified as 0.917 Å, with the corresponding charges on D and F (±0.414) chosen to give a DF dipole moment in agreement with that obtained from gas-phase density functional theory calculations. For CD_3CN, force constants were modified for the C-D stretches (from 4.766 to 4.955) and the C ≡N stretch (from 16.582 to 18.010) to give better agreement with the experimentally observed gas phase frequencies.[69] In addition, we modified the standard MMFF force-field setup to allow for the existence of (1) the F radical, (2) sp^2 hybridized radicals of the sort that occur in the CD_2CN co-product, and (3) the CD_2CND^+ and CD_3CND^+ valence states.

The off-diagonal matrix elements H_{ij} (modelled using a functional form described later) are responsible for coupling together diagonal diabatic states *i* and *j* in Fig 3. State 2 in particular couples to the proton transfer state of every solvent molecule, and we assumed that the coupling parameters describing these interactions were identical (i.e., the coupling has the form of H_{24}) regardless of the solvent molecule's identity. We further assumed that the functional form and parameter values of H_{24} are identical to those of H_{23}. This was motivated by recognizing that proton transfer energies on the cyano end of acetonitrile are largely insensitive to whether the opposite carbon is sp^2 or sp^3 hybridized.

In the results presented below, we describe the reactive dynamics of an F radical embedded in 62 solvent molecules, giving a 64 × 64 $\mathbf{H}(\mathbf{q})$ matrix. The computational cost of these simulations is just over 64 times as large as the cost of running a typical simulation which only involves one state. The decision to utilize a 64-state matrix was determined through consideration of the number of CPU cores which we could reasonably exploit on the architectures available to us, the minimum size of the simulation required to quench DF without unduly heating the bath, and the fact that the our computational resources consisted of 8-core CPU nodes. To reduce the time required to complete any given simulation, we implemented a parallelized dynamics propagation strategy schematically illustrated in Fig 4. The propagation algorithm works by instructing each diabatic state to calculate its energy and forces in parallel as a separate thread within the MPI (message passing interface) framework. The results for each state are then gathered together to construct the matrix elements for $\mathbf{H}(\mathbf{q})$ in Eq (1), which is subsequently diagonalized, i.e.:

$$\mathbf{D} = \mathbf{U}^{\mathrm{T}}\mathbf{H}\mathbf{U} \qquad (2)$$

where $\mathbf{D}$ is a diagonal matrix containing the eigenvalues, λ, and $\mathbf{U}$ is a matrix containing the corresponding eigenvectors. The adiabatic ground state energy is taken as λ_0, the lowest

eigenvalue of **D**; the corresponding eigenvector $\mathbf{U}_0$ contains the coefficients describing how each diabatic basis state contributes to the state with energy λ_i. Application of the Hellman-Feynman relation then gives a matrix of Cartesian atomic forces **F:**

$$\mathbf{F} = -\frac{d\mathbf{D}}{d\mathbf{q}} = \mathbf{U}^{\mathrm{T}} \frac{d\mathbf{H}}{d\mathbf{q}} \mathbf{U} \tag{3}$$

where $\mathbf{F}_0$ is a vector containing those forces which correspond to the lowest eigenvalue. $\mathbf{F}_0$ and λ_0 are then dispatched to each MPI process, overwriting the force and energy data on each process. Each process then propagates forward a single dynamical timestep; the identical forces and energies ensure that each process propagates to an identical geometry. At the new geometry, each process carries out its own energy and force calculations, the results of which are specific to the connectivity of the particular diabatic state. Because force calculations are the most expensive part of classical MD propagation schemes, this parallelized propagation strategy scales nearly linearly so long as a large enough multi-core architecture is available. The only additional cost is that required to diagonalize the Hamiltonian matrix and calculate the Hellman-Feynmann forces at each time step, which is negligible for the present size of system.

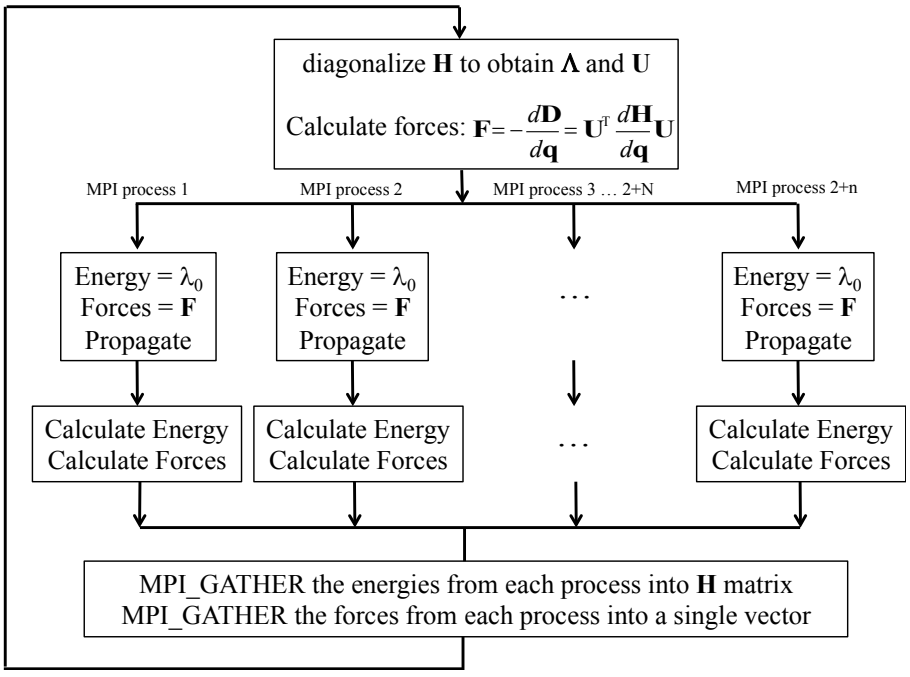

Figure 4: MPI parallelized MS-EVB propagation scheme

The trickiest aspect of the EVB method involves finding an appropriate functional form and parameter values for the off-diagonal matrix elements, H_{ij}. In our previous work, we modelled these off-diagonal elements using 1d Gaussian functions of interatomic distance. We tested the same approach for the F abstraction energies in this system – i.e., with a 1d Gaussian which was a function of the F-D distance. However, functional forms of this type yielded relatively poor fits

to the CCSD(T) PESs shown in Fig 2. To obtain satisfactory fits, we instead utilized two-dimensional ellipsoid Gaussian functions of the form:

$$H_{12}(r_1,r_2) = A_{12}\exp\left(-(a(r_1-r_1^0)^2 + 2b(r_1-r_1^0)(r_2-r_2^0) + c(r_2-r_2^0)^2)\right) \quad (4)$$

where r_1 is the interatomic D–F distance, r_2 is the interatomic C–D distance, A_{12} is the Gaussian amplitude, and r_0^1 and r_0^2 the respective reference values of r_1 and r_2. The *a, b,* and *c* parameters are defined as follows:

$$\begin{aligned} a &= \frac{\cos^2\theta}{2\sigma_{r1}^2} + \frac{\sin^2\theta}{2\sigma_{r2}^2} \\ b &= -\frac{\sin 2\theta}{4\sigma_{r1}^2} + \frac{\sin 2\theta}{4\sigma_{r2}^2} \\ c &= \frac{\sin^2\theta}{2\sigma_{r1}^2} + \frac{\cos^2\theta}{2\sigma_{r2}^2} \end{aligned} \quad (5)$$

where θ is the Gaussian rotation angle, and σ_{r1}, σ_{r2} are the respective widths in the r_1 and r_2 directions. In the post-reaction complexes, we found no advantage of the Eq (4) ellipsoidal Gaussians over a 1d Gaussian of the form

$$H_{23}(r) = H_{24}(r) = A_{24}\exp\left(-\frac{1}{2}([r-r_0]/\sigma)^2\right) \quad (6)$$

where r is the DF interatomic distance, r_0 is the Gaussian center, A_{24} is the amplitude, and σ is the width. Our observation that a 2d Gaussian provides little advantage over a 1d Gaussian indicates that, within the post-reaction complex, the change in diabatic character is closely correlated to the change of a single coordinate (the DF distance). This is distinct from the abstraction region of the potential, where the change in diabatic character is better correlated with the change in two coordinates (both of included in a 2d Gaussian coupling element).

To determine the values of the Gaussian parameters in Eq (4) – (6), we implemented a Levenberg-Marquardt nonlinear least squares algorithm to fit to the CCSD(T) results shown in Fig 2. The merit function used to determine goodness of fit was:

$$\chi^2(\text{parameters}) = \sum_{q \in \text{scan points}} \left[\frac{\lambda_0(\mathbf{q}) - (E_{CCSD(T)}(\mathbf{q}))}{E_{CCSD(T)}(\mathbf{q})}\right]^2 \quad (7)$$

with both $E_{CCSD(T)}$ and λ_0 referenced to the zeros specified in Fig 2. For the 2d Gaussian in Eq (4) – (5), the EVB parameters included A_{12}, θ, σ_{r1}, σ_{r2} r_0^1 and r_0^2; for the 1d Gaussian in Eq (6), the EVB parameters included A_{24}, r_0, and σ. Additional float parameters included ε_1 and ε_2 in Eq (1), to give the correct reaction energy. Using this methodology, fits to the fluorine-deuterium atom abstraction pathway, obtained for geometries scanned over C-D and F-D distances, are shown in

Fig 2. Fits in the post-reaction CD_3CN-DF complex, obtained by sampling over geometries with varying CN-DF and CND-F distances, are also shown in Fig 2. In both cases, the MS-EVB model is able to capture very well the topological features of the CCSD(T) PES. The root mean squared (RMSD) average error between CCSD(T) points and the fitted MS-EVB points along the Fig 2 abstraction path is 1.05 kcal mol^{-1}; the RMSD in the vicinity of the post-reaction complex is 2.10 kcal mol^{-1}. The final set of optimized parameters is given in Table 3, and the frequencies of the key stationary points are given in Table 4.

Table 3: best fit parameters obtained from non-linear least squares fitting of the MS-EVB model to the CCSD(T) results. units are [a]kcal mol^{-1}; [b]radians; [c]Å

H_{12} (2d Gaussian)		H_{24} (1d Gaussian)	
A_{12} [a]	96.6	A_{24} [a]	36.8
θ [b]	0.161	σ □	0.306
σ_{r1} [c]	0.311	r_0 [c]	1.22
r_0^1 [c]	1.61	-	-
σ_{r2} [c]	1.84	-	-
r_0^2 [c]	4.18	-	-

Table 4: Vibrational frequencies (in cm^{-1}) of species involved in the F + CD_3CN reaction (same species as Table 2), obtained using the MS-EVB force field by diagonalization of the relevant Hessian matrices.

Species	MS-EVB force field
DF	3000
CD_3CN	407, 407, 801, 811, 811, 1026, 1026, 1102, 2101, 2243, 2243, 2271
CD_2CN	328, 409, 526, 840, 881, 1104, 2169, 2307, 2333
CD_2CN–DF	34, 35, 183, 320, 337, 354, 423, 531, 840, 885, 1106, 2169, 2301, 2333, 2617
CD_3CN–DF	28, 28, 211, 360, 360, 423, 423, 811, 811, 811, 1026, 1026, 1104, 2101, 2243, 2243, 2270, 2652

Using the MS-EVB PES with the optimized parameters in Table 3, Fig 5 shows the results of a relaxed 1d scan along the minimum energy abstraction pathway. The results reveal a forward classical reaction barrier (i.e., without zero point energy correction) of 2.5 kcal mol^{-1}, in good agreement with the classical transition state barrier height predicted by our CCSD(T) calculations. Our decision not to include zero point energy in the fitted PES is motivated by two considerations. First, it is difficult to get a meaningfully smooth ZPE in those regions of Fig 2 far from stationary points. Second, previous studies comparing IVR rates obtained from both quantum dynamics (QD) and classical MD, suggest that a purely classical framework (i.e., classical trajectories run on a non-ZPE corrected PES, along with initial conditions which do not include ZPE) produces results in closest agreement to QD.[70, 71] Fig 5 also shows a relaxed 1d scan in the post-reaction region of the CD_2CN-DF potential, revealing a post-reaction complex with a stabilization energy of just over 7 kcal mol^{-1}, which again agrees well with the results in Table 1. We also used the MS-EVB model to carry out a 2d scan over the C-D and F-D distances in the post reaction CD_3CN-DF complex. The results, given in the SI, reveal a very similar PES topology for the

CD_3CN-DF and CD_2CN-DF complexes. This shows transferability in the functional form of the coupling elements as well as the values of the optimized parameters.

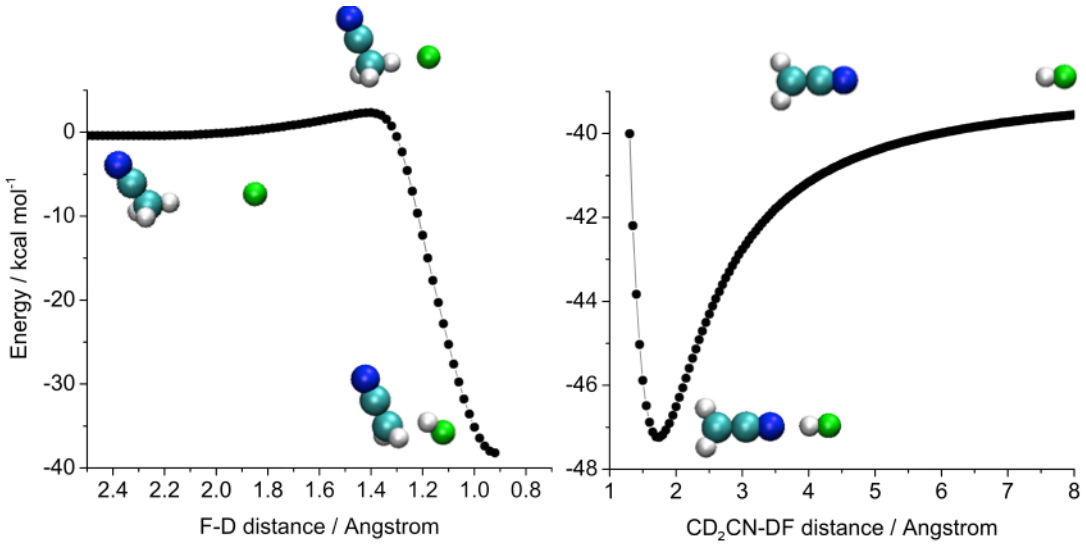

Figure 5: relaxed scans along the MS-EVB PES. Left hand panel shows results for a relaxed scan along the F-D distance in the F + $CD_3CN \rightarrow$ DF + CD_2CN reaction; right hand panel shows results for a relaxed scan along the CD_2CN-DF distance in the post-reaction complex (which are essentially identical to those for CD_3CN-DF). The line shown on the plot is an interpolation of the calculated energies.

Dynamics Simulations

Methods & Software

All of the dynamics work described in this paper was carried out using a locally modified version of the CHARMM software suite, to which we recently added general routines and an associated input structure that allows the user to specify MS-EVB Hamiltonians with matrix elements which are linear combinations of 2d Gaussians, 1d Gaussians, and/or constants. Fitting was carried out using a script to interface CHARMM with the Levenburg-Marquardt algorithm implementation available within the scientific python (SciPy) library. The diagonal elements of the Hamiltonian matrix were calculated using the Merck Molecular force-field (MMFF) in CHARMM,[68] modified as discussed above.

All dynamics simulations began with thermostatted NVT equilibration runs using the leapfrog Verlet integration scheme. These were used to generate initial conditions for subsequent NVE trajectories, propagated using a velocity Verlet algorithm. The discussion below makes reference to several different types of simulations, in which we simulated: (1) gas-phase DF as a Morse oscillator at different initial energies; (2) *non-equilibrium vibrational relaxation dynamics* (NE-VRD), in which DF is vibrationally excited according to the Frank-Condon principle within a microsolvation environment initially at equilibrium; (3) *non-equilibrium post-reaction solvation dynamics* (NE-PRSD), where DF (with zero excess vibrational energy beyond thermal) is placed

in a non-equilibrium microsolvation environment corresponding to that which immediately follows D abstraction (i.e., as shown in the middle panel of Fig 1); and (4) *non-equilibrium reaction dynamics* (NE-RxD) simulations, where the F radical abstracts a D atom to create vibrationally excited DF that subsequently relaxes. All solute/solvent simulations were carried out in a periodic cubic box with edge lengths of 17.8 Å. Nonbonded interactions were attenuated beyond a distance of 6.5 Å, and fully turned off beyond 8.5 Å.

NE-VRD simulations were carried out using 100 separate simulations with DF solvated within a periodic box including 61 CD_3CN molecules and one CD_2CN molecule, in line with the experimental density of acetonitrile (0.79 g/mL at room temperature). Equilibration runs of 100 ps (0.5 fs timestep) with a dissipative Langevin thermostat (friction coefficient of 10 ps^{-1}, and a heat bath of 300 K) were used to generate an ensemble of initial coordinates and velocities. These coordinates and velocities were used as starting points for subsequent NVE trajectories, with a duration of 10 ps (0.1 fs timestep). Before launching the NVE trajectories, Frank-Condon excitation of the DF was achieved by giving the velocity of the D atom in DF a non-equilibrium 'kick' of ~35 kcal mol^{-1} in the direction of its bonded fluorine neighbor using a local-mode approach.[71] This quantity of energy roughly corresponds to a DF vibrational quantum number of 4, in the limit that all of the excess energy available following (R1a) is deposited in the product DF. To generate equilibrium solute/solvent spectra, we carried out 50 simulations identical to those described above, with the exception that no initial non-equilibrium kick to the D atom was implemented.

NE-RxD simulations were carried out by initializing simulations with an F radical embedded in 62 CD_3CN solvent molecules. 200 separate trajectory simulations were carried out using equilibration runs of 100 ps (0.5 fs timestep) with a dissipative Langevin thermostat (friction coefficient of 10 ps^{-1}, and a heat bath of 300 K). The coordinates and velocities generated in these trajectories were used to launch subsequent NVE trajectories, with a duration of 20 ps (0.1 fs timestep). To guarantee that every one of the NVE trajectories resulted in a reaction and thereby improve the statistics of the analyses carried out below, we exploited the recently developed BXD algorithm.[55, 72, 73] BXD is a formally exact extension of transition state theory (TST), which conserves energy and is particularly well suited to accelerating reactive events in studies such as this through the addition of configuration space constraints. So long as the distance between the constraints and the transition state is larger than the system's characteristic dynamical decorrelation length, then a BXD-accelerated simulation gives meaningful statistics following transition state passage.[72] In non-equilibrium studies like that outlined herein, this is a considerable advantage of BXD compared to other biasing methods – e.g., umbrella sampling,

where the biasing has the consequence that the dynamical results are no longer meaningful in non-equilibrium regimes.[55, 72] During the equilibration runs, we specified BXD constraints to ensure that the distance between the fluorine radical and the reactive D had a lower bound of 1.5 Å and an upper bound of 1.8 Å, enclosing a region well to the reactant side of the abstraction TS. This prevented the reactants diffusing away from one another while still preserving interactions with the neighboring solvent molecules. In the NVE runs, the lower bound BXD constraint was removed, accelerating the rate of transition state passage and resulting in every trajectory undergoing an abstraction event, usually within 0.5 ps of the first timestep.

Upon their completion, all of the trajectories described above were examined to ensure that they satisfied energy conservation to within better than 1% of the average total kinetic energy (i.e., less than 1 kcal mol^{-1}). It is not uncommon that dynamics simulations carried out utilizing multi-state EVB methods fail to conserve energy, owing to an incomplete basis set of valence states in Eq (1). Because our simulations included all possible couplings for a specified valence state (i.e., $\mathbf{H}(\mathbf{q})$ included the interaction of DF with all possible solvent molecules), they were not subject to this source of error. For example, every equilibrium trajectory conserved energy within the specified acceptability threshold. The reaction and relaxation dynamics, on the other hand, *were* subject to energy conservation problems; however, the MS-EVB model was not the source of these failures. Rather, they arose because of the large amount of energy (~35 kcal mol^{-1}) initially localized in the DF stretching motion, together with the relatively large time step chosen. As a result, ~20% of the reaction and relaxation dynamics trajectories failed to conserve energy properly and were excluded from the analyses described below.

Time dependent energies of DF were determined using the strategy outlined in previous work.[13, 17] Briefly, DF's time-dependent Cartesian velocities, $\dot{\mathbf{q}}(t)$, (obtained from non-equilibrium NVE trajectories) were projected into the translational, rotational, and vibrational normal modes of DF in its center-of-mass frame equilibrium geometry, $\mathbf{q}_{eq}$, as follows:

$$\dot{\mathbf{Q}}(t) = \mathbf{L}^{-1}\dot{\mathbf{q}}(t) \tag{8}$$

where $\dot{\mathbf{Q}}(t)$ is a vector of normal mode velocities, and $\mathbf{L}$ is a 3N × 3N matrix obtained from diagonalizing the mass-weighted Hessian of DF (with column vectors corresponding to the Cartesian displacements of DF's 3 translations, 2 rotations, and single vibration). The kinetic energy of the ℓth normal mode, $\mathbf{T}^{\ell}(t)$, is determined as

$$\mathbf{T}^{\ell}(t) = \sum_{i\alpha} \frac{m_i}{2}[\mathbf{L}^{\ell}_{i\alpha}\dot{\mathbf{Q}}^{\ell}(t)]^2 \tag{9}$$

where m is the atomic mass, i runs over the atom indices, and α runs over the Cartesian x, y, z directions. In this notation, the column vectors in **L** have been transformed from mass-weighted to Cartesian space, and normalized using the appropriate constant, N_ℓ. Unlike the potential energy, the kinetic energy is diagonal in the normal mode displacements. The virial theorem specifies that, on average, the total energy is equipartitioned between kinetic and potential contributions, so that the average total energy in some mode over a particular time window τ, may be calculated as:

$$\left\langle \mathbf{E}^{\ell}(t) \right\rangle \approx 2\left\langle \mathbf{T}^{\ell}(t) \right\rangle_{\tau} \tag{10}$$

where the angled brackets indicate averages. All reported values of the DF stretching energy obtained in this work used Eq (10). So long as τ spans several vibrational periods of the stretching mode, then Eq (10) may be expected to give reasonably accurate results.[74] For analysis of the DF stretch, the averaging was carried out with τ = 250 fs. Strictly speaking, the virial theorem applies only to harmonic vibrations; however, we conducted a number of tests which showed that it gives accurate results when applied to the vibrationally excited anharmonic DF Morse oscillator modelled herein (even at high energies where the anharmonicity is largest).

The spectra reported in the analysis that follows were obtained from the well-known relationship that links a power spectrum to the Fourier transform of some dynamical observable $C(t)$:[28, 29, 75]

$$I(\omega) = \frac{1}{2\pi} \int_{-\infty}^{+\infty} C(t) \exp(-i\omega t) dt \tag{11}$$

Eq (11) is often cast in an alternative form that permits one to utilize fast Fourier algorithms to obtain power spectra from dynamical observables which have a finite time duration, $2T$:[28, 29, 75, 76]

$$I(\omega) = \frac{1}{2\pi} \lim_{T\to\infty} \frac{1}{2T} \left\langle \left| \int_{0}^{2T} C(t) \exp(-i\omega t) dt \right|^2 \right\rangle \tag{12}$$

where the angled brackets indicate an average over trajectories launched with different sets of initial conditions. In this work, $C(t)$ was taken to be the velocity autocorrelation function, i.e., $< v(0) \cdot v(t) >$ where v is a vector containing all the velocities of a relevant set of atoms. The spectral results reported herein utilize a sampling frequency of 1 fs (i.e., sampling every 10 time steps), which according to the Nyquist theorem, allows us to detect periodic motion with frequencies of ~16,000 cm^{-1} or less. The spectral resolution of Eq (12) depends on how long of a time window, $2T$, is spanned by the correlation function (longer time spans allow increasingly fine resolution). All time-dependent spectra were calculated from correlation functions with a length of 1.024 ps (i.e., $2T$ = 1024 fs). In those plots which include a sequence of time-dependent

spectra obtained from a sequence of correlation functions, individual spectra are indexed by the midpoint of the time window spanned by $C(t)$ (e.g., the spectrum obtained from the correlation function spanning 0 to 1.024 ps is referred to as the '0.512 ps' spectrum).

To aid interpretation of the transient DF spectra obtained using Eq (12), we utilized a nonlinear least squares minimization procedure to fit the raw spectra, $I(\omega)$, to a sum of Gaussian functions as follows:

$$I(\omega) = \sum_{i=1,2} A_i \exp\left[-\frac{(\omega - \omega_i^0)^2}{2\sigma_i^2} \right] \tag{13}$$

where A_i is the amplitude of Gaussian function i, σ_i is its corresponding width, and ω_i^0 is the position of its center. At most, we carried out fitting using two Gaussian functions ($i = 1, 2$), which adequately captured the DF features obtained using Eq (12). In general, a single Gaussian was sufficient to capture the transient behavior of the dominant DF stretching peak which is the emphasis of this work. The utility of the two-Gaussian approach is its ability to capture a small spectral feature to the blue of the main DF stretching feature, which we observed in a number of simulations. This small feature corresponds to DF which is not engaged in a solvent hydrogen bonding complex. In the text that follows, we refer to the results obtained from the one-Gaussian fits. The SI includes results obtained from two-Gaussian fitting.

In addition to time-dependent spectra, we also report time-dependent radial distribution functions (RDFs) to analyze transient changes in the DF solvent environment. Those presented below were obtained by averaging together the RDFs obtained from separate trajectories. Individual RDFs for a given trajectory were obtained by calculating interatomic distances every femtosecond (i.e., every 10 timesteps), placing them in data arrays of length 1024, and subsequent histogramming of the 1024 member data arrays. All reported RDFs were constructed using histogram bins of 0.05 Angstrom. Normalization of each RDF was carried out following averaging.

Anharmonic PES and Dynamics of the DF Morse Oscillator

The time-dependent DF spectra obtained from reaction dynamics simulations of (R1) are the result of a complex set of competing effects, the first of which concerns the anharmonicity of the DF stretching mode. Indeed, it is the anharmonicity in the DF stretch which permits experimental identification of transient vibrational excited states. From the quantum mechanical perspective, allowed transitions between adjacent vibrational states in a Morse oscillator have an energy which decreases linearly with increasing vibrational quantum state.[77] Consequently, adjacent transitions at higher vibrational states lie to the red of transitions at lower lying

vibrational quantum states. From the classical perspective used here, where vibrational eigenstates are not quantized, the vibrational energy content in the Morse oscillator is on a continuum; however, the vibrational frequency of the oscillator red shifts with increasing energy owing to the importance of large amplitude anharmonic motions.

Classical approaches are unable to capture the quantized transitions between vibrational eigenstates which occur in quantum mechanical approaches, with the net result that spectra obtained from classical simulations lack the finer structure seen in quantum mechanical approaches. However, such structures are often washed out in condensed phase systems, and previous work has shown that the classical approach to calculating diatomic vibrational spectra can often provide line shapes which agree well with those obtained in both quantum mechanical calculations and experimental observations.[28, 29] For systems in their ground vibrational state, there is a well-known systematic error in the peak locations calculated from classical spectra compared to their quantum mechanical counterparts, which may be easily corrected by a simple energy shift formula.[28, 29] Anharmonicity is the principal source of this error: a classical oscillator has an energy on the order of k_BT, meaning that it is confined to a largely harmonic region at the bottom of the Morse potential, whereas a quantum oscillator has a minimum energy which corresponds to its $v = 0$ zero point (i.e., several times k_BT). Observed spectral features primarily arise from transitions between $v = 0$ and $v = 1$, meaning that the quantum oscillator therefore samples larger regions of the anharmonic PES compared to the classical system. The extent of disagreement between the classical and quantum mechanical approaches is therefore most dramatic at low energies – i.e., close to the thermal regime. In this work, where the DF is produced from chemical reaction with substantial vibrational excitation ($v \sim 2 - 3$), then: (1) the initial vibrational energy content in the nascent DF will be very similar whether it is treated classically or quantum mechanically; and (2) detailed balance requires that downward transitions will dominate compared to upward transitions. Consequently, in condensed phase regimes with oscillators that have a high initial energy, and so long as the ensemble-averaged downward transition rates are approximately equal in the classical and quantum simulations, it is reasonable to suppose that the classical and quantum mechanical systems will explore similar regions of the anharmonic PES, giving a smaller deviation between classical and quantum mechanical spectra.

A common theoretical approach for calculating vibrational energy relaxation (VER) rate coefficients from state i to j is to split the simulation into 'system' and 'bath' components. The coupling which allows energy to flow between the system and bath is the Fourier transform of the quantum correlation function of the ij system matrix coupling element.[30, 78] However, accurate calculation of the quantum time correlation is extremely difficult for all but the smallest systems.

Hence, a more common approach is to replace the quantum time correlation function with a classical time correlation function, with the subsequent application of a quantum correction factor (QCF). For ground state vibrational transitions, a number of formulas have been derived which provide QCFs to classical vibrational energy relaxation results.[27, 30, 78, 79] For low energy $v = 1 \leftarrow 0$ transitions, the quantum correction factors are often small, (on the order of 2 – 3) so long as one takes care to use reasonably accurate force fields.[27, 78] Given that VER is notoriously sensitive to the system-bath coupling, it is therefore usually difficult to determine whether discrepancies between calculated VER and experimental VER in condensed phase systems arise from the QCF, or from errors in the potential.[30] For higher energy transitions, the form of the QCF remains subject to substantial uncertainty.

The uncertainties in the form that the QCF should take for higher lying transitions, coupled with the added complexity as a result of the fact that the transient high energy states which we are investigating arise from a chemical reaction event, led us to utilize a purely classical approach. QCFs act to increase the rate of VER compared to the classical result; therefore, our results provide a lower limit on the rate at which DF relaxes in CD_3CN solvent. As shown in what follows, our results agree very well with the available experimental data, but the complexities of the system under investigation, combined with the experimental errors, make it difficult to quantitatively assess the relative importance of small QCFs.

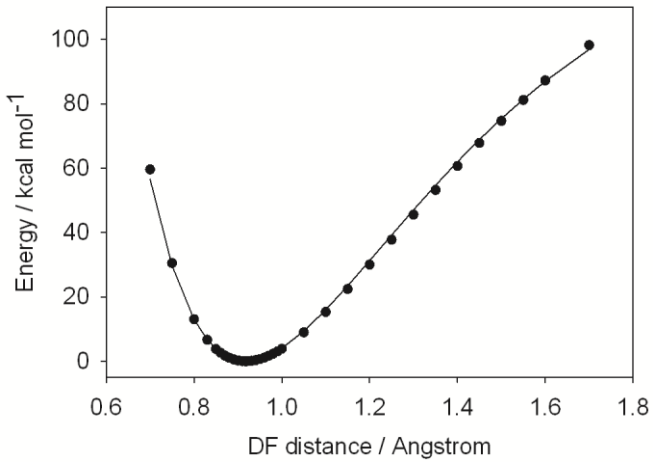

Figure 6: comparison between CCSD(T)-F12b/aug-cc-pVTZ calculations along the DF stretch coordinate, and the Eq (12) analytical Morse function used in the dynamics simulations

To represent DF as a Morse oscillator, we added a subroutine to CHARMM which allows the user to select any given harmonic bond and assign it a standard Morse form:

$$V(r) = D_e(1 - \exp(-a(r - r_e)))^2$$
$$a = \sqrt{k_e / D_e} \qquad (14)$$

where r is the bond distance, D_e is the bond dissociation energy, r_e is the equilibrium bond distance, and the relationship between a and k_e can be seen through a Taylor series expansion of Eq (14). The value of k_e was set to 9.657 millidyne Å^{-1}. With this value of k_e, the frequencies at the bottom of the Morse well, v_0 (obtained by diagonalization of the diatomic Hessian) for HF and DF are 4138 cm^{-1} and 3000 cm^{-1}, respectively, in close agreement with the corresponding experimental gas-phase values of 4138 cm^{-1} and 2998 cm^{-1}.[80] The value of D_e, determined from fitting to CCSD(T)-F12b/aug-ccpVTZ calculations at a set of structures near the minimum, was set at 141.28 kcal mol^{-1}. Fig 6 shows a comparison between ab initio energies at a range of DF geometries, calculated at the CCSD(T)-F12b/aug-cc-pVTZ level, and the corresponding analytic form for the Morse potential (Eq 14) implemented within CHARMM for use in these simulations. We verified that energy-dependent vibrational frequencies obtained using Eq (12) to analyze gas phase MD simulations of the Fig 6 Morse curve agreed with the well-known analytical expression describing Morse frequencies – i.e., $v(E) = v_0\sqrt{(D_e - E)/D_e}$.[77, 81] Further details on these comparisons are available in the SI.

Non-Equilibrium Vibrational Relaxation Dynamics (NE-VRD)

We carried out a range of NE-VRD simulations to investigate relaxation dynamics of a DF Morse oscillator solute in a CD_3CN bath (i.e., R1b, without any reaction). Initially we tested the simplest possible PES – i.e., nothing beyond the standard electrostatic and van der Waals non-bonded terms in the MMFF force field. Relaxed scans on this PES show a post-reaction complex with an energy of ~8 kcal mol^{-1}, like that in Fig 5. Going back to early work (outlined by Rapp[82] and Yardley[83] for example), several experimental and theoretical studies have shown that vibration-to-vibration (V-V) energy transfer depends strongly on (1) spectral overlap between the donor and acceptor, and (2) the donor/acceptor coupling. Spectral analysis of MD simulations reveals CD_3CN bands between ~2000 – 2340 cm^{-1} (with well-defined peaks near 2101 cm^{-1} and 2247 cm^{-1}, discussed later in relation to Fig 10), which correspond to the CN stretching frequency.

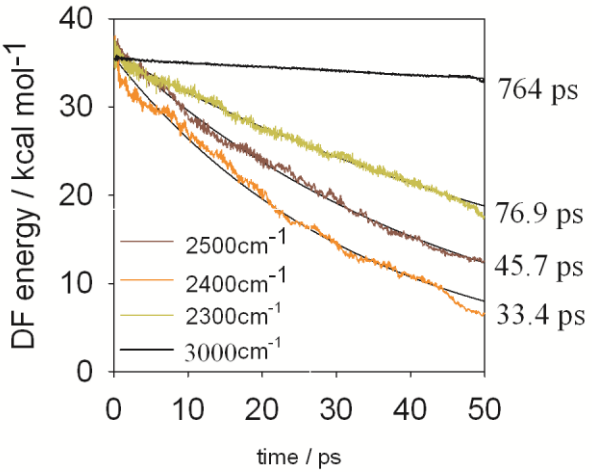

Figure 7: Sensitivity of DF relaxation to the DF force constant in NE-VRD simulations. The plots show the relaxation time profiles of DF vibrational energy into the CD_3CN solvent, for force constants which give ν_0 values of 3000 cm^{-1}, 2500 cm^{-1}, 2400 cm^{-1}, and 2300 cm^{-1}. In all tests, ~35 kcal mol^{-1} vibrational energy was initially localized in the DF stretch. The numbers to the right of the plot show the time constants obtained by fitting each curve to a single exponential decay

To quantitatively probe the dependence of DF energy relaxation on the energetic separation between the DF frequency and the CD_3CN solvent bands, we carried out a sensitivity analysis of energy transfer as a function of the DF force constant. The results, shown in Fig 7, were obtained by averaging over different sets of 10 trajectories with ~35 kcal mol^{-1} initially localized in the DF stretch, and then fitting to a single exponential function. Inspection of Fig 7 confirms that the rate of energy relaxation from DF into the CD_3CN solvent increases as the DF frequency approaches that of the CD_3CN solvent bands. A DF force constant which reproduces the experimental gas phase vibrational frequency of 3000 cm^{-1} gives extremely slow energy relaxation, with a time constant on the order of 764 ps. Decreasing the DF force constant increases the DF energy relaxation rate: the maximum relaxation rate has a time constant of ~33.4 ps, for a DF frequency of 2400 cm^{-1} . Further decreases in the DF force constant increase its energetic separation from the CD_3CN bands, and lead to a slower rate of energy transfer; i.e., a DF frequency of 2300 cm^{-1} gives a relaxation rate with a time constant of ~76.9 ps.

Fig 7 highlights the dynamics shortcomings of the standard non-bonded terms in the MMFF force field: (1) the DF relaxation rates are substantially slower than the timescales suggested by the experimental results;[11] and (2) adjusting the D-F force constant to tune the energy relaxation rate is ultimately unsatisfactory because it recovers neither the gas-phase experimental vibrational frequency, nor the large experimental solvatochromatic shift. Fig 8 highlights the principal reason for these shortcomings. For geometries in the $CD_3CN\cdots DF$ complex, it shows a comparison between relative CCSD(T) energies with those obtained utilizing only the standard non-bonded terms in the MMFF force field (DF Morse oscillator with ν_0 = 3000 cm^{-1}). At low energies (i.e., in the vicinity of the $CD_3CN\cdots DF$ minimum energy, with DF distances close to 0.92 Å), there is good agreement between the MMFF and CCSD(T) relative energies. However, in

regimes with elongated D–F distances and decreased N···D distances, the agreement is substantially worse. The MMFF force field underpredicts the amount of coupling, giving energies which are too large. In fact, such large DF interatomic distances are accessible when the DF has significant vibrational excitation on the order of 2 – 3 quanta, so that the use of standard coupling terms leads to significant errors in the potential energy, which in turn appears to be the cause for the large underestimate of the rate of energy transfer.

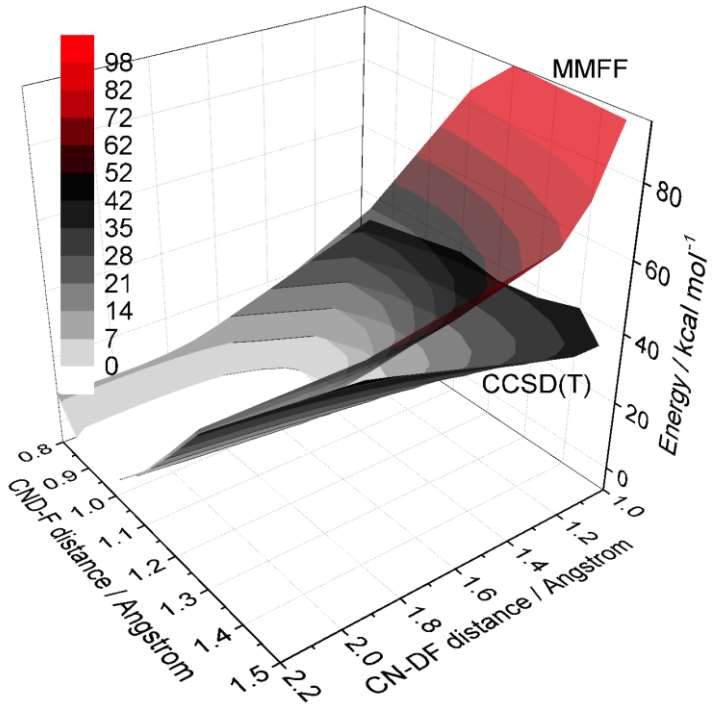

Figure 8: Energies in the region of the post-reaction $CD_3CN\cdots DF$ complex, obtained as a function of both the D–F and the N···D distance (as in Fig 2). The plot shows energies evaluated using CCSD(T) electronic structure theory, and those obtained using the MMFF force field (with DF treated as a Morse oscillator). MMFF has higher energies because it considerably underestimates CH_3CN-DF coupling away from the minimum. (PES energy reference is the same as in Fig 2.; color scale units are in kcal mol^{-1})

It was in fact the results in Fig 7 and Fig 8 which led us to the Eq (1) force field shown in Fig 2, allowing us to include solvent/solute coupling which is missing in the standard MMFF non-bonded terms. Fig 9 shows the DF relaxation profile which results from utilizing the Eq (1) force field (~35 kcal mol^{-1} initial excitation energy, same as the Fig 7 initial conditions). The decay is substantially faster than any of the curves in Fig 7. Within the first few vibrational periods of the initially excited DF, 5 – 6 kcal mol^{-1} of its initial energy is rapidly transferred to solvent, which accounts for why Figs 7 and 9 appear to have different energies at time zero. Whereas the Fig 7 results were well-fit using a single exponential function, the DF VER profile in Fig 9 shows multiple relaxation regimes – fast relaxation at short times with a time constant of ~0.49 ps, and a long-time relaxation rate with a time constant of ~5.0 ps. These relaxation timescales are 2 – 3 orders of magnitude faster than those obtained for the comparable 3000 cm^{-1} curve in Fig 7. The

Fig 9 results were obtained using a DF force constant that reproduces the gas-phase DF frequency of 3000 cm^{-1}; however, the treatment of solute/solvent coupling means that we also reproduce the ~400 cm^{-1} solvatochromatic shift experimentally observed between isolated DF and DF in CD_3CN solvent. Fig 10 shows the equilibrium power spectrum of DF in CD_3CN solvent (obtained from equilibrium simulations of DF in CD_3CN with thermal initial conditions). The peak corresponding to the DF stretch occurs at 2540 ± 30 cm^{-1}, in reasonable agreement with results obtained from experimental IR spectroscopy,[11, 84, 85] which indicate a position of ~2580 cm^{-1}.

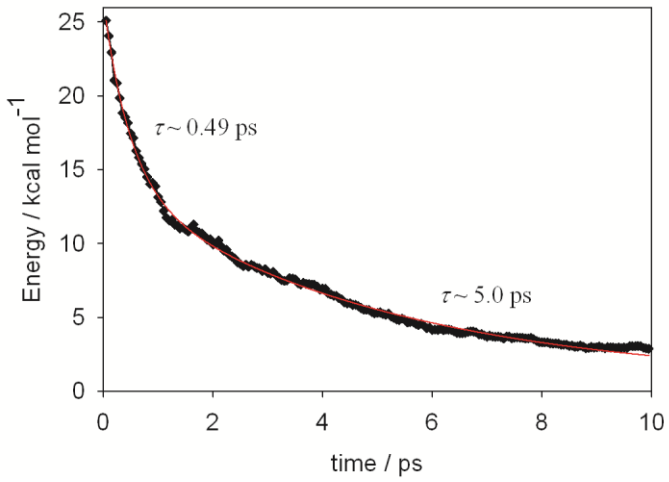

Figure 9: time-profile obtained from NE-VRD simulations, showing the vibrational energy content of DF solute in CD_3CN solvent, utilizing 64 × 64 EVB matrix in Eq (1). Biexponential fits to the relaxation profile clearly show two distinct regimes – fast relaxation at short times, and slower relaxation at long times

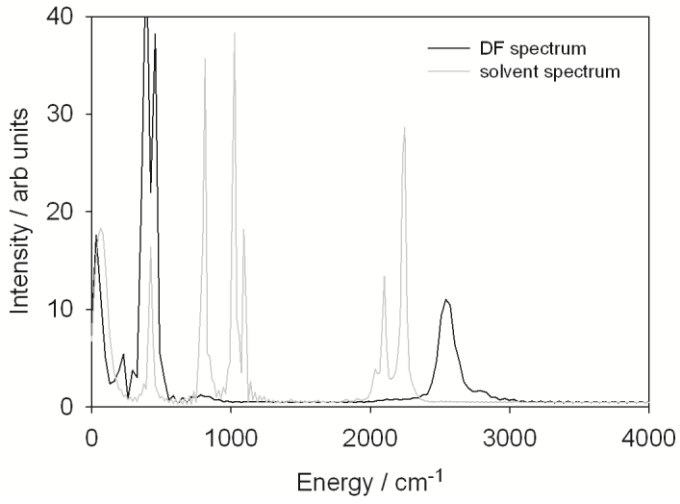

Figure 10: Equilibrium spectra of CD_3CN solvent, and DF embedded in CD_3CN solvent. Note that the DF spectral data has been arbitrarily scaled to clarify its spectral features; otherwise it is dwarfed by the relative magnitudes of the solvent peaks. The DF spectral peak can be well fit with a single Gaussian centered at 2540 cm^{-1}.

The multiple timescales observed in the Fig 9 DF relaxation profile can be partly rationalized through inspection of the time dependent spectra obtained following DF excitation, shown in the top panel of Fig 11. Black lines show the DF vibrational spectra and grey lines show

the equilibrium solvent spectrum. Red lines show fits to the DF stretching feature using a single Gaussian function, while green lines show fits carried out using the sum of two Gaussian functions. The time-dependent results of this fitting procedure are shown in the bottom panels of Fig 11 (The SI contains additional snapshots of the time dependent spectra, along with plots showing the parameters returned from the two-Gaussian fits at every snapshot). In the immediate aftermath of excitation (i.e., at times less than a picosecond), DF undergoes large amplitude vibrational motion resulting in a transient spectrum with a band center of ~2211 cm^{-1} (i.e., red shifted by over 300 cm^{-1} from its equilibrium position) and a width of ~293 cm^{-1}. This results in a very strong overlap with the solvent bands at 2101 and 2247 cm^{-1}. Combined with the strong coupling that arises from large amplitude DF motion, this results in extremely fast energy relaxation. As the DF cools with time, Fig 11 shows that the DF band sharpens and blue shifts toward its equilibrium position. Thus solvent/solute spectral overlap decreases along with the probability of large amplitude DF motions that strongly couple to solvent. The combination of these two effects yields a time dependent decrease in the energy relaxation rate from the DF solute to the CD_3CN solvent, although we cannot rule out the possibility that longer timescale solvation dynamics might also play a role during the relaxation process.[86, 87]

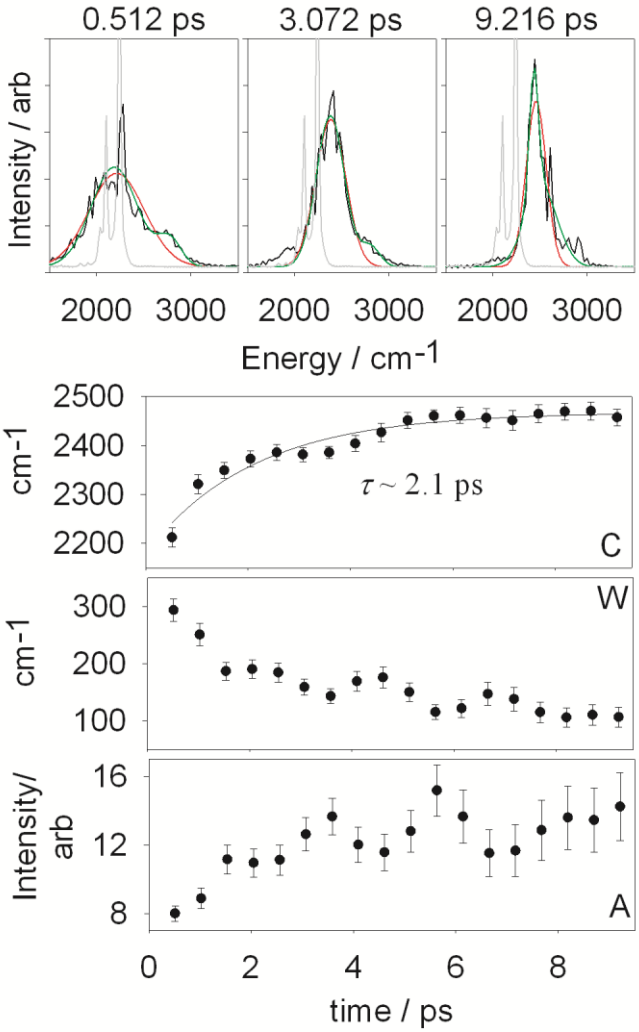

Figure 11: Top panel shows time dependent spectra of DF in the NE-VRD simulations. The different time slices were obtained by averaging over 1.024 ps time windows to obtain the CD_3CN vibrational spectrum (grey) and the DF vibrational spectrum (black). The red and black lines are fits to the DF vibrational spectrum, using one and two Gaussian functions, respectively. Bottom panels show results obtained from fitting the time dependent DF (relaxation) spectra with Eq (13) using a single Gaussian. Plots show the Gaussian centre (C), width (W), and amplitude (A). The time series for the peak center (C) was fit to a single exponential of the form $y = A\exp(-t/\tau)+C$

Non-Equilibrium Post-Reaction Solvation Dynamics (NE-PRSD)

The NE-VRD dynamics discussed in the previous section, carried out with Frank-Condon excited DF in a microsolvation environment initially at equilibrium, were critical in assessing how the solvent/solute potential energy function outlined in Eq (1) captures important dynamical observables related to DF relaxation. However, given that the ultimate aim of this work is to understand the combined DF reaction/relaxation dynamics, it is important to recognize that, when DF is produced from a chemical reaction, its vibrational energy content is not the only observable in a non-equilibrium regime – its microsolvation environment is also in a non-equilibrium regime, and constitutes an important transient dynamical feature.[17]

To specifically examine the post-reaction solvation environment the DF experiences immediately following the abstraction event (and in the absence of complicating effects due to vibrational cooling), we carried out NE-PRSD simulations. The initial conditions for these

simulations were obtained by running reactive dynamics simulations in which the vibrational excitation of the nascent DF was damped immediately following the abstraction event (i.e., at the moment of first passage through the DF equilibrium geometry), modifying the deuterium velocity in the vibrational frame so as to remove all non-thermal vibrational excitation. This yielded a set of trajectories where the initial coordinates of the solute and solvent are sampled from the distribution that follows in the immediate wake of the abstraction reaction, but with a thermal distribution of velocities for the CD_3CN solvent and DF solute. In the NE-PRSD simulations, any time-dependence observed in the DF spectrum may be assigned to relaxation of the non-equilibrium post-reaction microsolvation environment in which DF is embedded immediately following its formation. Fig 12 shows spectra of DF in the picoseconds following abstraction for these NE-PRSD trajectories, along with results from fitting the time dependent spectra to a single Gaussian function. The SI contains additional snapshots of the time dependent spectra, along with plots showing the parameters returned from the two-Gaussian fits at every snapshot. At very short times, the DF band is centered at 2758 $cm^{-1.}$ It quickly relaxes to the equilibrium value of 2540 cm^{-1} on a timescale of ~0.58 ps. The peak is very broad at short times, and sharpens rapidly following reaction to a characteristic width of ~100 cm^{-1}.

These NE-PRSD trajectories show the rapidly changing nature of the DF spectrum at short times following reaction, resulting from relaxation of the post-reaction microsolvation environment. The distribution of geometries required to facilitate a reaction means that – immediately following formation – the DF has not yet had time to form intermolecular complexes with the solvent. In this sense, it feels a microsolvation environment which is somewhere between the equilibrium limit (i.e., engaging in solvent hydrogen bonds), and the gas-phase limit. The utility of these NE-PRSD trajectories is that they allow us to deconvolute spectral shifts linked to vibrational excitation and relaxation versus those which arise from a dynamic zero-excitation baseline as DF's post-reaction microsolvation environment relaxes.

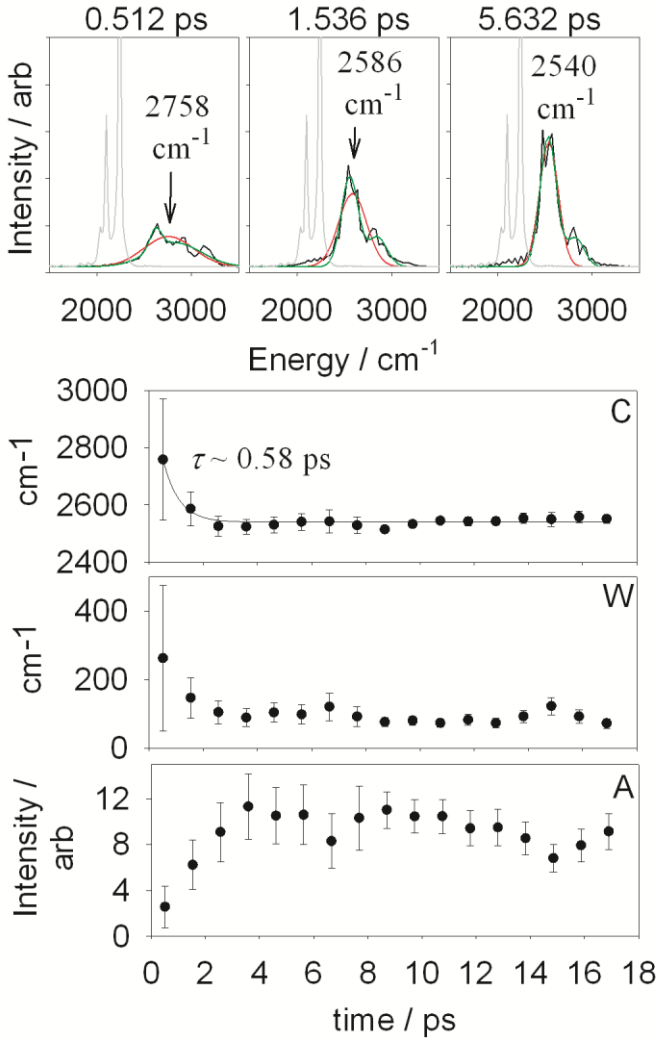

Figure 12: Time-dependent spectra of DF from the NE-PRSD trajectories; the observed time-dependence reflects the relaxation of DF's post-reaction microsolvation environment. The panels and the corresponding line colors are identical to those described in the Fig 11 caption. The single-Gaussian peak centre in panel (C) has been fit to a single exponential decay.

Non-Equilibrium Reaction Dynamics (NE-RxD)

In what follows, we discuss the results obtained from full NE-RxD simulations, rationalizing them in terms of the results that have been presented so far. In the NE-RxD simulations, vibrational excitation of the nascent DF arises from energy deposition following abstraction of a D atom by fluorine from a CD_3CN solvent molecule. Fig 13 shows the time-dependent DF relaxation profile obtained following the abstraction event (where time zero is defined as the point at which DF undergoes first passage through its equilibrium bond distance). According to our simulations, the initial abstraction reaction deposits ~23 kcal mol^{-1} vibrational energy into the DF stretch. In the harmonic approximation, one quantum of DF stretch energy corresponds to ~8.6 kcal mol^{-1}, such that the classical vibrational quantum number of the nascent DF in our simulations is somewhere between 2 and 3. Fitting the Fig 13 data with a biexponential function yields a reasonable fit with two different timescales – fast relaxation at short times with

a time constant of ~1.04 ps, and a long-time relaxation rate which is slower by a factor of ~10, with a relaxation time constant of ~11.3 ps.

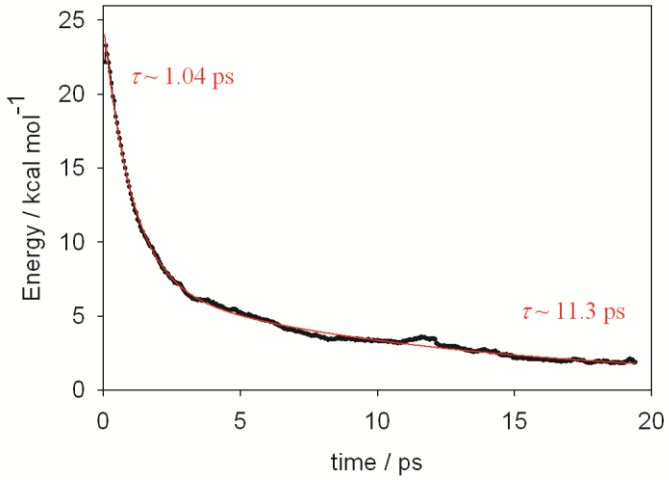

Figure 13: time-profile for vibrational energy content of DF solute in CD_3CN solvent in the NE-RxD simulations, utilizing the previously discussed 64 × 64 EVB matrix. Relaxation timescales obtained with a biexponential fit are shown in red.

Fig 14 shows the time dependent spectrum of DF following abstraction. The SI contains additional snapshots of the time dependent spectra, along with plots showing the parameters returned from the two-Gaussian fits at every snapshot. At short times – i.e., less than a picosecond – the transient DF spectrum has a width of ~280 cm^{-1}, and a peak centered at 2473 cm^{-1}; it is to the red of its equilibrium position at 2540 cm^{-1}, and to the blue of the solvent spectrum peaks at 2101 and 2247 cm^{-1}. As time goes on and the DF cools, Fig 14 shows that the DF band sharpens and blue shifts toward its equilibrium position at 2450 cm^{-1}. This results in a decrease of both solvent/solute spectral overlap and the probability of large amplitude DF motions that strongly couple to solvent molecules. These two effects combine to decrease the energy relaxation rate from the DF solute to the CD_3CN solvent as time increases. The order of magnitude difference in the relaxation rates at short and long times (shown in Fig 13) is very similar to that observed in Fig 9. The timescales for DF relaxation in Fig 13 are longer by nearly a factor of two compared to those shown in Fig 9, which appears to be linked to the fact that the vibrationally excited DF in the NE-RxD simulations has poorer spectral overlap with the CD_3CN solvent bands than DF excited in the NE-VRD simulations.

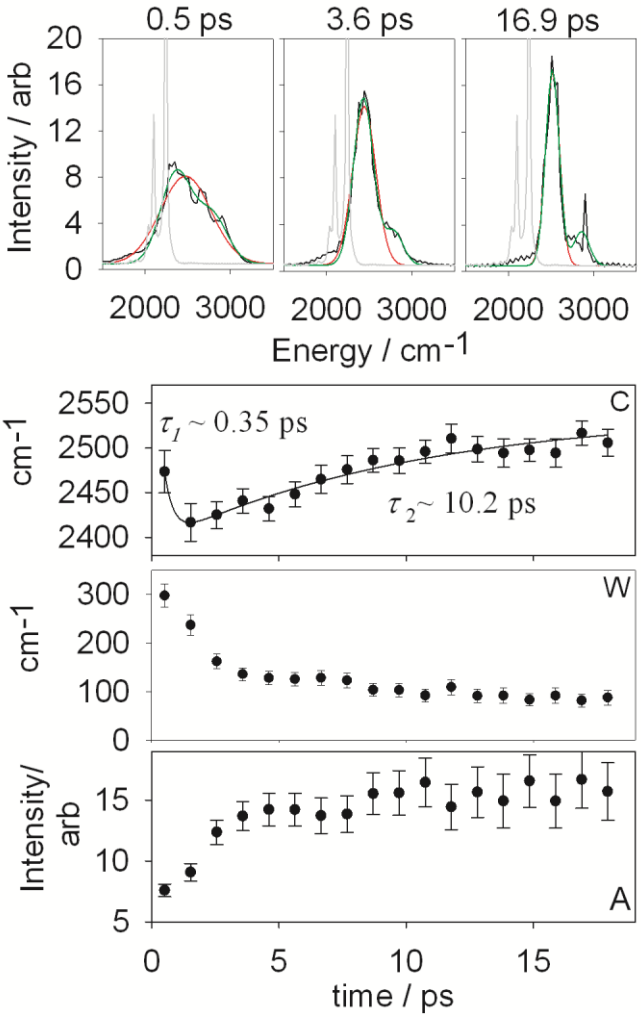

Figure 14: Top panel shows time dependent power spectra of nascent DF in the NE-RxD simulations (at 0.5, 1.6, and 16.9 ps). The bottom three panels show the results obtained from fitting the time dependent DF band using Eq (13) with a single Gaussian. Panels C, W, and A, show the time-dependent Gaussian centre, width, and amplitude, respectively. The line in panel C corresponds to fitting results obtained using Eq (16)

The spectral time profile of DF in the NE-RxD simulations shown in Fig 14 (panel C) is markedly distinct from that obtained in the NE-VRD simulations in Fig 11 (panel C). In the NE-VRD simulations, DF's transient spectral features are easy to rationalize: as a result of vibrational excitation, there is a prompt displacement to the red in the DF band, from 2211 cm^{-1} ← 2540 cm^{-1} [this 329 cm^{-1} displacement is close to the ~300 cm^{-1} displacement we would expect from gas phase simulations of a Morse oscillator (see SI)]. Following this prompt displacement, there is a gradual blue shift back to the equilibrium band center (2540 cm^{-1}) as the excited DF loses its vibrational energy, and the time-dependence of the band position (shown in Fig 11 panel C) is well represented using a single exponential function.

In the NE-RxD simulations, the DF spectral position in Fig 14 (panel C) shows a rather more complicated time profile, with two important differences: (1) the initial prompt displacement to the red gives a DF band centered at 2473 cm^{-1}, far less deep into the red than the initial value of 2211 cm^{-1} in Fig 11; and (2) the DF band center undergoes a transient red shift at short times,

going through a minimum of 2416 cm^{-1} before blue shifting back toward equilibrium. To better understand these timescales, the results in Fig 14 (panel C) were fit using a biexponential function of the form

$$\omega_0(t) = A\exp(-t/\tau_1) - B\exp(-t/\tau_2) + C \quad (16)$$

with C fixed to the equilibrium DF band position (2540 cm^{-1}). The fit gave values of $\tau_1 \sim 0.35$ ps and $\tau_2 \sim 10.2$ ps, whose physical interpretations are discussed in further detail below. The complicated time dependence in Fig 14 (panel C) arises because – in the case of the NE-RxD simulations – the zero-excitation spectral baseline with respect to which shifts occur is not constant, on account of the fact that the post-reaction microsolvation environment of the DF relaxes, as discussed in the previous NE-PRSD section.

Fig 15 shows a time series of radial distribution functions (RDFs) between the D atom in DF, and the N atoms in the CD_3CN solvent molecules. The aim of these plots is to furnish insight into differences in solvent structure for DF relaxation in the NE-VRD simulations versus relaxation that follows in the wake of a chemical reaction (i.e., in the NE-RxD simulations). The RDFs for DF relaxation in the NE-VRD simulations reveal a distinct shift in peak position with time, from 1.50 Angstroms at short time to 1.65 Angstroms at long time. This well-defined shift is consistent with DF which remains hydrogen-bonded to solvent molecules during the relaxation process, and is easy to rationalize in terms of DF oscillator anharmonicity: at high vibrational energies, the average DF bond length is longer, which corresponds to a smaller average CD_3CN–DF distance. Consistent with this hypothesis is the fact that the time-dependent RDFs are essentially identical beyond distances of ~2 Å. The RDFs obtained following reaction (i.e., in the NE-RxD simulations) have a rather different profile. The distinguishing feature is not a peak shift, but rather the width of the distribution: at short times, the distribution is considerably wider than at longer times, with substantial amplitude at distances larger than 2 Å. This provides strong evidence for the fact that the nascent DF created following an abstraction reaction sees a wider range of microsolvation environments than those it sees in the NE-VRD simulations, where the microsolvation environment is initially at equilibrium.

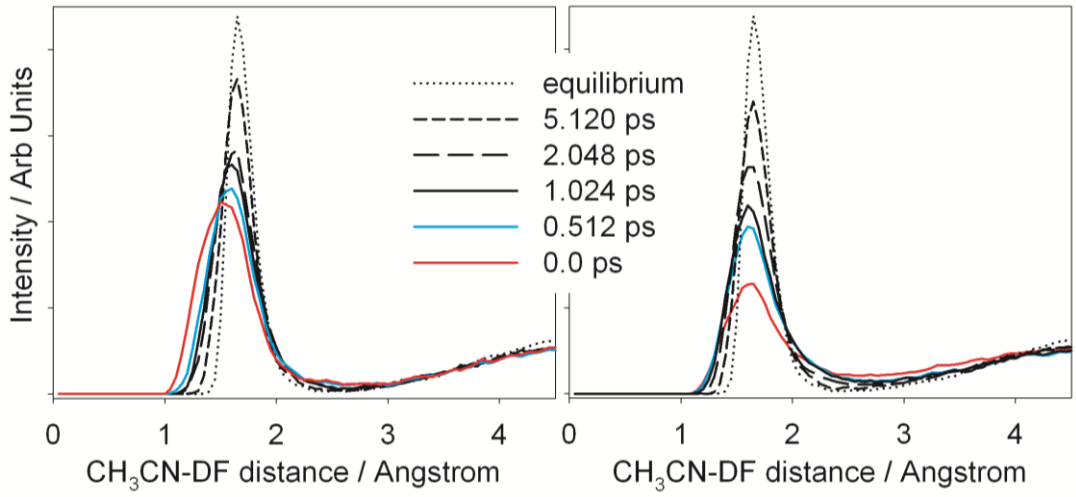

Figure 15: Time dependent RDFs obtained following vibrational relaxation of DF*. The left hand panel shows the RDF obtained when DF* relaxes in the NE-VRD simulations; the right hand panel shows the RDF obtained when DF* relaxes after being produced from chemical reaction (i.e., in the NE-RxD simulations).

Fig 16 synthesizes many of the results in the previous sections, in an effort to provide insight into the time profile of the DF band center in Fig 14 (panel C). The left hand panel of Fig 16 shows the NE-VRD relaxation profile of the DF band center, with a micro-solvation environment initially at equilibrium, characterized by complexes between the DF and solvent molecules (the left hand panel of Fig 15). The Frank-Condon vibrational excitation (illustrated in Fig 16 with a red arrow) can be imagined to displace the baseline toward the red at time zero, and subsequent vibrational relaxation of the DF results in a transient blue shift back to equilibrium (illustrated in Fig 16 with blue arrows), giving the curve shown in Fig 14C.

The right hand panel of Fig 16 shows the rather distinct time profile of the DF band center following reaction (from the NE-RxD simulations). At very short times, DF's post-reaction microsolvation environment is intermediate between the gas phase and the equilibrium limit, with a zero-excitation baseline of ~2758 cm^{-1}. Chemical reaction deposits vibrational excitation in the DF, resulting in a prompt displacement to the red of approximately 285 cm^{-1}, giving a band center at ~2473 cm^{-1}. The magnitude of this displacement is very similar to that observed in the NE-VRD simulations (and similar to what we predict for a gas phase Morse oscillator). The prompt displacement takes DF less far into the red than occurs in the NE-VRD simulations (2211 ← 2540 cm^{-1}, also shown in Fig 16), but farther into the red than occurs for the gas phase dynamics (2707 ← 2998 cm^{-1}, see SI). The origin of these differences is the zero-excitation spectral baseline of the DF stretch: in the gas phase, the zero-excitation baseline band center is 2998 cm^{-1}; in the NE-VRD simulations, the DF baseline center is 2540 cm^{-1}; and in the reactive case, the NE-PRSD simulations show that the time zero baseline center is 2758 cm^{-1} owing to an initially non-equilibrium post-reaction microsolvation environment. Following the prompt red shift, there are then two competing effects. A fast red shift occurs as the DF post-reaction microsolvation

environment relaxes, and DF undergoes rotational and translational motion to form Hydrogen bonded complexes with neighboring solvent molecules. The time constant for this shift is on the order of 0.35 ps (τ_1 in Fig 14C), in good agreement with the post-reaction microsolvation relaxation timescales seen in the NE-PRSD trajectories (Fig 12). There is also a blue shift with a time constant on the order of 10.2 ps (τ_2 in Fig 14C), which occurs as DF loses its vibrational energy to the solvent. The time-dependent spectral profile of the band center for the nascent DF formed following reaction is the result of these opposing effects – i.e., red shift due to relaxation of the DF's post-reaction microsolvation environment and blue shift due to dissipation of DF's vibrational energy.

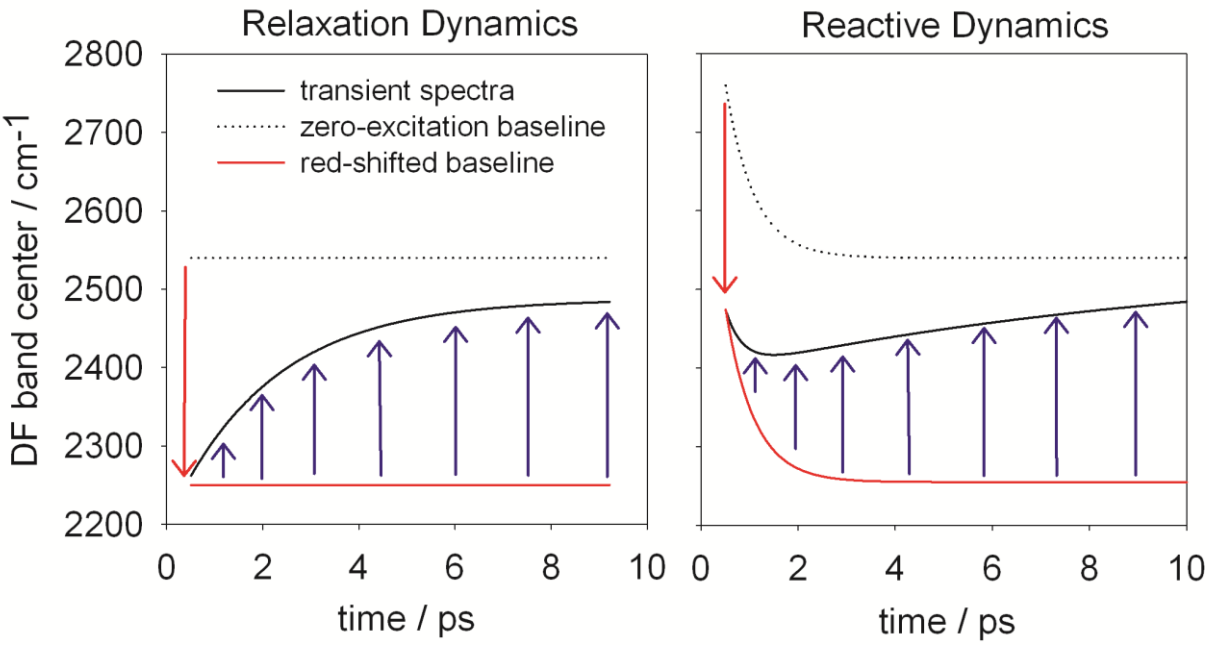

Figure 16: schematic diagram illustrating the contrasting DF spectral time profiles (black line) seen for DF* relaxation in the NE-VRD simulations (left panel, schematic of Fig 11C) versus DF* relaxation in the NE-RxD simulations that follows chemical reaction (right panel, schematic of Fig 14C). The dotted line illustrates the zero-excitation spectral baseline (i.e., position of the center), and the red solid line shows the spectral baseline displaced to the red as a result of prompt DF vibrational excitation at time zero (red arrow). Blue arrows show the blue shift that occurs as DF relaxes to equilibrium, losing its vibrational energy to the solvent.

Conclusions

In this article, we have described in detail a parallel MS-EVB implementation which we have used to investigate non-equilibrium reaction dynamics of F + CD_3CN abstraction reactions in CD_3CN solvent. Our approach captures several different experimental observables across both equilibrium and non-equilibrium regimes. In the equilibrium regime, it reproduces the experimental solvatochromatic spectral shift of DF in CD_3CN compared to its gas phase spectrum. In the non-equilibrium regime, it predicts a significant quantity of vibrational energy deposition (v = 2 – 3) in the nascent DF following abstraction, it also predicts energy relaxation timescales for excited DF which are in good agreement with those observed experimentally, and it also

captures time-dependence in the transient vibrational spectra of DF following reaction.[11] Our MD simulations also provide microscopic insight into dynamics that occur on timescales which are faster than what the experiments can resolve. In particular, the transient DF spectra show two competing effects that occur in the immediate wake of reaction: a blue shift linked to vibrational relaxation, and a red shift linked to relaxation of the DF's post-reaction microsolvation environment. This is distinct from what is observed when DF relaxation occurs following Frank-Condon excitation in a bulk solvent microsolvation environment initially at equilibrium – i.e., where the spectra show only a blue shift as a result of vibrational relaxation in the excited DF.

An accurate treatment of dynamics in the present system required substantially larger EVB matrices than in our previous solution phase reaction dynamics studies. This is partially a result of the fact that the quantity of vibrational excitation in the DF produced from (R1) is very large, and therefore large amplitude vibrational motions are likely to take the system far from equilibrium. In this non-equilibrium regime, the PES is very anharmonic, owing to strong solute-solvent coupling. A particularly interesting observation that has arisen from this study is the fact that we duplicate neither the experimentally measured spectra nor the vibrational relaxation timescales unless we include diabatic states with deuteron-transfer character in the multi-state Hamiltonian (i.e., as shown in Fig 3). Deuteron transfer states are most important for large amplitude DF motions, which create both strong solvent/solute spectral overlap as well as strong DF-solvent coupling. As DF relaxes, large amplitude motion is quenched, and both its spectral overlap with the solvent and its coupling to the solvent decrease in magnitude, resulting in a decrease in the DF relaxation rate as a function of time (e.g., in Figs 9 and 13).

The present study, where have investigated non-equilibrium reaction dynamics involving a solvent which is strongly coupled to the nascent solute, establishes an important limit that complements our previous studies of solution-phase reaction dynamics in weakly coupled solvents. Our results show that, even in a strong coupling regime, a thermal chemical reaction produces nascent products with considerable vibrational excitation, and that this excitation persists for an appreciable timescale. Our previous reaction dynamics studies of $CN + C_6H_{12}$ in dichloromethane solvent[13, 17, 18] examined how the post-reaction microsolvation environment impacts transient observables in the wake of a chemical reaction. In that work, we highlighted the difference between dynamics which occurs post-reaction, and that which occurs in bulk solvent and which would be predicted on the basis of linear response theory. In this study, we have similarly highlighted how the post-reaction solvation environment results in transient spectral profiles that are distinct from those observed in bulk solvent, as shown in Fig 16.

The framework we have described in this article, available within general MD packages

like CHARMM and TINKER, allows one to construct reactive force fields using multi-state molecular mechanics and EVB approaches, to carry out subsequent non-equilibrium MD simulations. It permits the use various force field approaches and utilities, along with a range of different functional forms for describing the coupling elements. In future work, it will be fascinating to explore the extent to which persistent vibrational excitation of the sort observed herein impacts reaction outcomes in more complex chemical systems,[12, 19] and also whether it is possible to build MS-EVB models by fitting to on-the-fly electronic structure theory using more sophisticated machine-learning strategies. We also plan to investigate whether the accuracy of the reactive potentials can be improved by building diabatic states from polarizable force fields, and whether such treatments provide further insight into reaction and relaxation processes in solution. Finally, we hope to examine alternative simulation approaches for obtaining accurate transient spectra of higher-energy vibrational quantum states which can be excited in exothermic chemical reactions.

Acknowledgements

DRG acknowledges support from the Royal Society as a University Research Fellow. AJOE recognizes financial support from the Engineering and Physical Sciences Research Council (EPSRC, Programme Grant EP/G00224X and a studentship for GTD) and the European Research Council (ERC, Advanced Grant 290966 CAPRI). JNH acknowledges a Royal Society Wolfson Merit Award covering some of the period when this work was performed.

References

1. J. C. Owrutsky, M. Li, B. Locke and R. M. Hochstrasser, J. Phys. Chem. **99**, 4842 (1995).
2. J. C. Owrutsky, D. Raftery and R. M. Hochstrasser, Annu. Rev. Phys. Chem. **45**, 519 (1994).
3. M. D. Fayer, *Ultrafast Infrared Vibrational Spectroscopy*. (CRC Press, 2013).
4. M. D. Fayer, *Ultrafast infrared and Raman spectroscopy*. (CRC Press, 2001).
5. T. Elsaesser and H. Van den Akker, *Ultrafast hydrogen bonding dynamics and proton transfer processes in the condensed phase*. (Springer Science & Business Media, 2013).
6. S. J. Harris, D. Murdock, Y. Y. Zhang, T. A. A. Oliver, M. P. Grubb, A. J. Orr-Ewing, G. M. Greetham, I. P. Clark, M. Towrie, S. E. Bradforth and M. N. R. Ashfold, Phys. Chem. Chem. Phys. **15**, 6567 (2013).
7. T. A. A. Oliver, Y. Zhang, M. N. R. Ashfold and S. E. Bradforth, Faraday Discussions **150**, 439 (2011).
8. L. Liu and H. J. Bakker, The Journal of Physical Chemistry B **119**, 2628 (2015).
9. V. Sundström, *Femtochemistry and Femtobiology: Ultrafast Reaction Dynamics at Atomic-scale Resolution: Nobel Symposium 101*. (Imperial College Press, 1997).
10. B. J. Gertner, R. M. Whitnell, K. R. Wilson and J. T. Hynes, J. Am. Chem. Soc. **113**, 74 (1991).
11. G. T. Dunning, D. R. Glowacki, T. J. Preston, S. J. Greaves, G. M. Greetham, I. P. Clark, M. Towrie, J. N. Harvey and A. J. Orr-Ewing, Science **347**, 530 (2015).
12. D. R. Glowacki, C. H. Liang, S. P. Marsden, J. N. Harvey and M. J. Pilling, J. Am. Chem. Soc. **132**, 13621 (2010).
13. D. R. Glowacki, A. J. Orr-Ewing and J. N. Harvey, The Journal of Chemical Physics **134**, 214508 (2011).
14. A. J. Orr-Ewing, D. R. Glowacki, S. J. Greaves and R. A. Rose, J. Phys. Chem. Lett. **2**, 1139 (2011).
15. R. A. Rose, S. J. Greaves, F. Abou-Chahine, D. R. Glowacki, T. A. A. Oliver, M. N. R. Ashfold, I. P. Clark, G. M. Greetham, M. Towrie and A. J. Orr-Ewing, Phys. Chem. Chem. Phys. **14**, 10424 (2012).
16. A. J. Orr-Ewing, J. Chem. Phys. **140** (2014).
17. D. R. Glowacki, R. A. Rose, S. J. Greaves, A. J. Orr-Ewing and J. N. Harvey, Nat. Chem. **3**, 850 (2011).
18. S. J. Greaves, R. A. Rose, T. A. A. Oliver, D. R. Glowacki, M. N. R. Ashfold, J. N. Harvey, I. P. Clark, G. M. Greetham, A. W. Parker, M. Towrie and A. J. Orr-Ewing, Science **331**, 1423 (2011).
19. B. K. Carpenter, J. N. Harvey and D. R. Glowacki, Phys. Chem. Chem. Phys. **17**, 8372 (2015).
20. J. Rehbein and B. K. Carpenter, Phys. Chem. Chem. Phys. **13**, 20906 (2011).
21. L. M. Goldman, D. R. Glowacki and B. K. Carpenter, J. Am. Chem. Soc. **133**, 5312 (2011).

22. D. R. Glowacki, S. P. Marsden and M. J. Pilling, J. Am. Chem. Soc. **131**, 13896 (2009).
23. Y. Oyola and D. A. Singleton, J. Am. Chem. Soc. **131**, 3130 (2009).
24. G. A. Voth and R. M. Hochstrasser, J. Phys. Chem. **100**, 13034 (1996).
25. J. T. Hynes, Annu. Rev. Phys. Chem. **36**, 573 (1985).
26. C. G. Elles and F. F. Crim, in *Annu. Rev. Phys. Chem.* (2006), Vol. 57, pp. 273-302.
27. J. L. Skinner and K. Park, J. Phys. Chem. B **105**, 6716 (2001).
28. P. H. Berens and K. R. Wilson, J. Chem. Phys. **74**, 4872 (1981).
29. P. H. Berens, S. R. White and K. R. Wilson, J. Chem. Phys. **75**, 1 (1981).
30. J. L. Skinner, Theor Chem Acc **128**, 147 (2010).
31. A. Yamada and S. Okazaki, J. Chem. Phys. **124**, 11 (2006).
32. J. R. Maple, U. Dinur and A. T. Hagler, Proceedings of the National Academy of Sciences **85**, 5350 (1988).
33. M. Gruebele and P. G. Wolynes, Accounts Chem. Res. **37**, 261 (2004).
34. F. Abou-Chahine, S. J. Greaves, G. T. Dunning, A. J. Orr-Ewing, G. M. Greetham, I. P. Clark and M. Towrie, Chemical Science **4**, 226 (2013).
35. Y. Y. Zhang, T. A. A. Oliver, M. N. R. Ashfold and S. E. Bradforth, Faraday Discussions **157**, 141 (2012).
36. T. J. Preston, M. A. Shaloski and F. F. Crim, J. Phys. Chem. A **117**, 2899 (2013).
37. O. F. Mohammed, S. Luber, V. S. Batista and E. T. J. Nibbering, J. Phys. Chem. A **115**, 7550 (2011).
38. R. Otto, J. Brox, S. Trippel, M. Stei, T. Best and R. Wester, Nat. Chem. **4**, 534 (2012).
39. M. A. Bellucci and D. F. Coker, J. Chem. Phys. **136**, 194505 (2012).
40. T. J. F. Day, A. V. Soudackov, M. Cuma, U. W. Schmitt and G. A. Voth, J. Chem. Phys. **117**, 5839 (2002).
41. U. W. Schmitt and G. A. Voth, J. Chem. Phys. **111**, 9361 (1999).
42. K. F. Wong, J. L. Sonnenberg, F. Paesani, T. Yamamoto, J. Vanicek, W. Zhang, H. B. Schlegel, D. A. Case, T. E. Cheatham, W. H. Miller and G. A. Voth, J. Chem. Theory Comput. **6**, 2566 (2010).
43. S. T. Roberts, A. Mandal and A. Tokmakoff, J. Phys. Chem. B **118**, 8062 (2014).
44. T. Nagy, J. Yosa Reyes and M. Meuwly, J. Chem. Theory Comput. **10**, 1366 (2014).
45. R. Jorn, J. Savage and G. A. Voth, Acc. Chem. Res. **45**, 2002 (2012).
46. M. Higashi and D. G. Truhlar, J. Chem. Theory Comput. **4**, 1032 (2008).
47. R. Bianco and J. T. Hynes, J. Chem. Phys. **102**, 7864 (1995).
48. P. M. Kiefer, E. Pines, D. Pines and J. T. Hynes, J. Phys. Chem. B **118**, 8330 (2014).
49. N. Boekelheide, R. Salomon-Ferrer and T. F. Miller, Proc. Natl. Acad. Sci. U.S.A. **108**, 16159 (2011).
50. Y. T. Chang and W. H. Miller, J. Phys. Chem. **94**, 5884 (1990).
51. H. B. Schlegel and J. L. Sonnenberg, J. Chem. Theory Comput. **2**, 905 (2006).
52. S. C. L. Kamerlin and A. Warshel, Wiley Interdiscip. Rev.-Comput. Mol. Sci. **1**, 30 (2011).
53. A. Warshel and R. M. Weiss, J. Am. Chem. Soc. **102**, 6218 (1980).
54. D. R. Glowacki, R. Lightfoot and J. N. Harvey, Mol. Phys. **111**, 631 (2013).
55. D. R. Glowacki, E. Paci and D. V. Shalashilin, J. Phys. Chem. B **113**, 16603 (2009).
56. B. R. Brooks, C. L. Brooks, III, A. D. Mackerell, Jr., L. Nilsson, R. J. Petrella, B. Roux, Y. Won, G. Archontis, C. Bartels, S. Boresch, A. Caflisch, L. Caves, Q. Cui, A. R. Dinner, M. Feig, S. Fischer, J. Gao, M. Hodoscek, W. Im, K. Kuczera, T. Lazaridis, J. Ma, V. Ovchinnikov, E. Paci, R. W. Pastor, C. B. Post, J. Z. Pu, M. Schaefer, B. Tidor, R. M. Venable, H. L. Woodcock, X. Wu, W. Yang, D. M. York and M. Karplus, J. Comput. Chem. **30**, 1545 (2009).
57. J. M. Bowman and G. C. Schatz, Annu Rev Phys Chem **46**, 169 (1995).
58. J. C. Polanyi, Science **236**, 680 (1987).
59. D. D. Dlott, Chemical Physics **266**, 149 (2001).
60. A. Tokmakoff, B. Sauter and M. D. Fayer, J. Chem. Phys. **100**, 9035 (1994).
61. Gaussian 09, Revision D.01, M. J. Frisch, G. W. Trucks, H. B. Schlegel, G. E. Scuseria, M. A. Robb, J. R. Cheeseman, G. Scalmani, V. Barone, B. Mennucci, G. A. Petersson, H. Nakatsuji, M. Caricato, X. Li, H. P. Hratchian, A. F. Izmaylov, J. Bloino, G. Zheng, J. L. Sonnenberg, M. Hada, M. Ehara, K. Toyota, R. Fukuda, J. Hasegawa, M. Ishida, T. Nakajima, Y. Honda, O. Kitao, H. Nakai, T. Vreven, J. A. Montgomery, Jr., J. E. Peralta, F. Ogliaro, M. Bearpark, J. J. Heyd, E. Brothers, K. N. Kudin, V. N. Staroverov, R. Kobayashi, J. Normand, K. Raghavachari, A. Rendell, J. C. Burant, S. S. Iyengar, J. Tomasi, M. Cossi, N. Rega, J. M. Millam, M. Klene, J. E. Knox, J. B. Cross, V. Bakken, C. Adamo, J. Jaramillo, R. Gomperts, R. E. Stratmann, O. Yazyev, A. J. Austin, R. Cammi, C. Pomelli, J. W. Ochterski, R. L. Martin, K. Morokuma, V. G. Zakrzewski, G. A. Voth, P. Salvador, J. J. Dannenberg, S. Dapprich, A. D. Daniels, Ö. Farkas, J. B. Foresman, J. V. Ortiz, J. Cioslowski, and D. J. Fox, Gaussian, Inc., Wallingford CT, 2009.
62. MOLPRO, version 2012.1, a package of ab initio programs, H.-J. Werner, P. J. Knowles, G. Knizia, F. R. Manby, M. Schütz, P. Celani, T. Korona, R. Lindh, A. Mitrushenkov, G. Rauhut, K. R. Shamasundar, T. B. Adler, R. D. Amos, A. Bernhardsson, A. Berning, D. L. Cooper, M. J. O. Deegan, A. J. Dobbyn, F. Eckert, E. Goll, C. Hampel, A. Hesselmann, G. Hetzer, T. Hrenar, G. Jansen, C. Köppl, Y. Liu, A. W. Lloyd, R. A. Mata, A. J. May, S. J. McNicholas, W. Meyer, M. E. Mura, A. Nicklass, D. P. O'Neill, P. Palmieri, D. Peng, K. Pflüger, R. Pitzer, M. Reiher, T. Shiozaki, H. Stoll, A. J. Stone, R. Tarroni, T. Thorsteinsson, and M. Wang, see http://www.molpro.net.
63. H.-J. Werner, P. J. Knowles, G. Knizia, F. R. Manby and M. Schütz, Wiley Interdisciplinary Reviews: Computational Molecular Science **2**, 242 (2012).
64. H. J. Werner, G. Knizia and F. R. Manby, Mol. Phys. **109**, 407 (2011).
65. I. S. Ufimtsev and T. J. Martínez, Comp. Sci. Eng. **10**, 26 (2008).
66. A. Sisto, D. R. Glowacki and T. J. Martinez, Accounts Chem. Res. **47**, 2857 (2014).
67. The decision to allow only one reactive deuterium is not an inherent limitation of our approach. By adding more states, it would have been possible to enable the fluorine to abstract any of the D atoms, albeit at a larger computational expense. Because the emphasis in this study is on the post transition-state dynamics that follow D

abstraction rather than association kinetics, the error arising from this simplification is relatively minor. As shown in the discussion of the dynamics results, a far more significant source of error arises if one neglects the coupling between the DF and its neighboring solvent molecules.

68. T. A. Halgren, J. Comput. Chem. **17**, 490 (1996).
69. T. Shimanouchi, *Tables of Molecular Vibrational Frequencies Consolidated. Volume I*. (National Bureau of Standards, Washington, DC, 1972).
70. S. K. Reed, D. R. Glowacki and D. V. Shalashilin, Chemical Physics **370**, 223 (2010).
71. D. R. Glowacki, S. K. Reed, M. J. Pilling, D. V. Shalashilin and E. Martinez-Nunez, Phys. Chem. Chem. Phys. **11**, 963 (2009).
72. D. R. Glowacki, E. Paci and D. V. Shalashilin, J. Chem. Theory Comput. **7**, 1244 (2011).
73. E. Martinez-Nunez and D. V. Shalashilin, J. Chem. Theory Comput. **2**, 912 (2006).
74. L. M. Raff, J. Chem. Phys. **89**, 5680 (1988).
75. D. W. Noid, M. L. Koszykowski and R. A. Marcus, J. Chem. Phys. **67**, 404 (1977).
76. M. Thomas, M. Brehm, R. Fligg, P. Vöhringer and B. Kirchner, Phys Chem Chem Phys **15**, 6608 (2013).
77. N. B. Slater, Nature **180**, 1352 (1957).
78. G. Stock, Phys. Rev. Lett. **102**, 118301 (2009).
79. D. Rostkier-Edelstein, P. Graf and A. Nitzan, J. Chem. Phys. **107**, 10470 (1997).
80. K.-P. Huber and G. Herzberg, *Constants of diatomic molecules*. (Springer, 1979).
81. P. M. Morse, Physical Review **34**, 57 (1929).
82. D. Rapp and T. Kassal, Chemical Reviews **69**, 61 (1969).
83. J. T. Yardley, *Introduction to molecular energy transfer*. (Academic Press, 1980).
84. K. Nakanishi, H. Touhara, H. Shimoda and N. Watanabe, The Journal of Physical Chemistry **75**, 2222 (1971).
85. G. L. Johnson and L. Andrews, The Journal of Physical Chemistry **87**, 1852 (1983).
86. S. J. Rosenthal, X. Xie, M. Du and G. R. Fleming, J. Chem. Phys. **95**, 4715 (1991).
87. M. Maroncelli, J. Chem. Phys. **94**, 2084 (1991).